Improving the Quality of MODIS LAI Products by Exploiting Spatiotemporal Correlation Information

Jingrui Wang, Kai Yan, Si Gao, Jiabin Pu, Jinxiu Liu, Taejin Park, Jian Bi, Eduardo Eiji Maeda, Janne Heiskanen, Yuri Knyazikhin, and Ranga B. Myneni

***Abstract*— The Moderate Resolution Imaging Spectroradiometer (MODIS) leaf area index (LAI) product is critical for global terrestrial carbon monitoring and ecosystem modeling. However, MODIS LAI is calculated on a pixel-by-pixel and day-by-day basis without using spatial or temporal correlation information, which leads to its high sensitivity of LAI to uncertainties in observed reflectance, resulting in an increased noise level in time series. While exploiting prior knowledge is a common practice to fill gaps in observations, little research has been conducted on reducing noisy fluctuations and improving the overall quality of the MODIS LAI product. To address this issue, we proposed a spatiotemporal information composition algorithm (STICA), which directly introduces prior spatiotemporal correlation and multiple quality assessment (MQA) information into the existing MODIS LAI product. STICA reduces the noise level and improves the quality of the product while maintaining the original physically based (radiative transfer model, RTM) LAI production process. In our analysis, the R^2 increased from 0.79 to 0.81 and the root-mean-square error (RMSE) decreased from 0.81 to 0.68 compared to the ground-based LAI reference. The improvement was more pronounced with the degradation of the data quality. STICA reduced noisy fluctuations in the LAI time series to varying degrees among eight biome types. In the Amazon forest, STICA significantly improved the time-series stability of LAI. Moreover, STICA can effectively eliminate abnormal declines in time series and correct for extreme outliers in LAI. We expect that the MODIS LAI reanalyzed product generated by this method will better support the application of high-quality LAI datasets.**

Manuscript received 5 February 2023; revised 16 March 2023; accepted 26 March 2023. Date of publication 3 April 2023; date of current version 13 April 2023. This work was supported in part by the National Natural Science Foundation of China Major Program under Grant 42192580 and in part by the National Natural Science Foundation of China under Grant 42271356. The work of Eduardo Eiji Maeda was supported by the Academy of Finland under Grant 318252, Grant 319905, and Grant 345472. *(Corresponding author: Kai Yan.)*

Jingrui Wang is with the School of Land Science and Techniques, China University of Geosciences, Beijing 100083, China (e-mail: jingruiwang@email.cugb.edu.cn).

Kai Yan, Si Gao, and Jinxiu Liu are with the Faculty of Geographical Science, Beijing Normal University, Beijing 100875, China, and also with the School of Land Science and Techniques, China University of Geosciences, Beijing 100083, China (e-mail: kaiyan.earthscience@gmail.com; gaosi_2021@email.cugb.edu.cn; jinxiuliu@cugb.edu.cn).

Jiabin Pu, Yuri Knyazikhin, and Ranga B. Myneni are with the Department of Earth and Environment, Boston University, Boston, MA 02215 USA (e-mail: om7759@bu.edu; jknjazi@bu.edu; ranga.myneni@gmail.com).

Taejin Park is with the NASA Ames Research Center, Moffett Field, CA 94035 USA (e-mail: taejin1392@gmail.com).

Jian Bi is with the College of Earth and Environmental Sciences, Lanzhou University, Lanzhou 730020, China (e-mail: bijian@lzu.edu.cn).

Eduardo Eiji Maeda and Janne Heiskanen are with the Department of Geosciences and Geography, University of Helsinki, 00014 Helsinki, Finland (e-mail: duardo.maeda@helsinki.fi; janne.heiskanen@helsinki.fi).

Digital Object Identifier 10.1109/TGRS.2023.3264280

***Index Terms*— Leaf area index (LAI), Moderate Resolution Imaging Spectroradiometer (MODIS), reanalysis, spatiotemporal information, spatiotemporal information composition algorithm (STICA), time-series stability (TSS).**

I. Introduction

LEAF area index (LAI), generally defined as the one-sided green leaf area per unit ground horizontal surface area in broadleaf canopies and as the projected needle leaf area in coniferous canopies [1], is a critical parameter for characterizing vegetation canopy structure and energy absorption capacity [2], [3]. LAI has been designated as an essential climate variable by the Global Climate Observing System (GCOS) due to its critical role as an input for a range of applications, such as numerical weather prediction, climate modeling, and forest monitoring [4], [5], [6]. Additionally, LAI plays a crucial role in regulating global water, carbon, and energy cycles [7], [8].

Moderate Resolution Imaging Spectroradiometer (MODIS) LAI is one of the most widely used LAI products thanks to its clear theoretical basis, relatively high temporal and spatial resolution, extensive historical time series, and open access policy [9]. This radiative transfer model (RTM)-based LAI product represents a milestone in Earth observations [10]. Not only the production of this product does not depend on other LAI datasets but is often used as a training dataset of other products [11], [12] and as the reference for product comparisons [13], [14]. Additionally, it has been widely used in terrestrial carbon monitoring [8], global ecosystem dynamic simulation [15], and studies on the relationship between vegetation dynamics and human activities [16], [17], [18].

The MODIS algorithm retrieves daily LAIs by ingesting daily red and near-infrared (NIR) bidirectional reflectance factors (BRFs) and biome maps [3]. Then, the temporal compositing approach is used to select the best retrievals and generate eight-day products from daily retrievals [10], [19]. Inversion values in this period are considered the candidate retrievals according to the principle that the main algorithm has the highest priority, whereas backup algorithm retrievals are selected when there is no main algorithm available [2]. The optimal LAI retrieval corresponds to the maximum fraction of photosynthetically active radiation absorbed by vegetation (FPAR) value within this period [20]. Hence, MODIS LAI retrievals are calculated independently for each pixel and on a daily basis, without considering spatial or temporal correlation information. Differences in the observation conditions of two

adjacent periods can cause substantial uncertainty in the LAI time series, which can inaccurately depict the actual growth trajectory of vegetation and limit its applications in forest simulations, crop-growth monitoring, and yield estimation research [21], [22]. Therefore, it is important to obtain a high-quality LAI time series.

There have been many studies aiming at reducing high-frequency noises and improving the temporal consistency of LAI, which can mainly be divided into reflectance-based and LAI-based approaches. The Global Land Surface Satellite (GLASS) LAI reprocessed MODIS reflectance data through filtering and interpolation algorithms to obtain smooth and continuous surface reflectance values. A generalized regression neural network was then used to retrieve LAI values from the reprocessed reflectance data [12]. Moreover, the reflectance was used as input data to obtain high-quality LAI in data assimilation methods for studying the carbon cycle characteristics of subtropical forest ecosystems [21], [23]. Indeed, the smoothness and consistency of an LAI time series can be improved by filtering the reflectance data and assimilating multisource data. However, these methods can hinder the quantification of factors associated with vegetation dynamics, bidirectional effects, and observation uncertainties, as well as lose the sun-sensor geometry information, challenging to employ physically based inversion algorithms. Another alternative is to improve the smoothness and consistency of LAI curves by adding prior knowledge (e.g., biome classification or spatial and temporal correlation information) into the LAI datasets. These methods can be divided into three categories depending on the information used.

1) *Spatially Based Method*: This is the most traditional and fundamental approach of the three kinds of methods, which uses the spatial measurements adjacent to the target point to predict values at any location. This approach assumes that surrounding data at spatial scales share the same geometric structure or statistics [24]. The typical representative is spatial interpolation, which can be applied using cubic splines [25], bilinear interpolation [26], inverse distance weight interpolation [27], and Kriging interpolation [28]. In addition, other representative methods include propagated diffusion methods [29], exemplar-based methods [30], and variation-based methods [31]. Most spatial-based methods are easy to implement and can be applied well to small areas. In addition, spatial-based methods are only suitable for utilization in areas with relatively simple distribution characteristics of biome types and generally have low accuracy in heterogeneous land cover regions.
2) *Temporally Based Method*: This is the most common technique and is directly connected with dynamic growth changes of vegetation, replacing low-quality data with simple means of averaged contemporaneous values or from adjacent times [32], [33] and substituting local gaps caused by clouds or atmospheric aerosols with multiple consecutive adjacent values [34]. Methods also include the maximum values composite (MVC) [35], the best index slope extraction (BISE) using a sliding window to remove outliers [36], and the iterative interpolation method [37]. In addition, temporal filtering methods are also widely used in LAI time-series smoothing, including the Savitzky–Golay (SG) filter [38], the moving average (MA) filter [39], the asymmetric Gaussian (AG) function fitting [40], double logistic (DL) function fitting [41], and harmonic analysis of time series (HANTS) [42]. Curve fitting can capture vegetation dynamics well, but is also susceptible to local fluctuations and data noise [43]. Furthermore, many current LAI time-series production methods are based on temporal deep learning models such as neural networks, random forests, and decision trees [44], [45], [46].
3) *Hybrid Method*: Each of the above two approaches has advantages and weaknesses, which rely on only one correlation. As a result, they are outstanding in some cases but powerless in others. Accordingly, combining their respective strengths can avoid most of the weaknesses. The hybrid method comprehensively considers the correlation in the spatial and temporal domains and makes up for the lack of single information to achieve more robust results [47], [48]. In recent years, a growing body of research has confirmed that combining multiple information has enormous advantages over using a single feature [49], [50], [51], [52]. Borak and Jasinski [53] evaluated several temporal and spatial interpolation methods using MODIS LAI time series, and the results indicate that the underlying land cover can affect the accuracy of individual interpolation methods. However, a combination of spatial and temporal methods provides superior interpolative capabilities to any single approach. Similarly, a study comparing various interpolation methods found that combining space and time was less affected by environmental factors such as terrain and climate [54].

Spaceborne remote sensors have the capability to rapidly supply large-area observations, which provide the only way to monitor and observe phenology over large scales and at regular intervals [55]. With the growing number of Earth observation satellites, more LAI products are developed. Smoothing of LAI time series is often used to fill gaps in observations caused by cloud cover or sensor failures. However, there is little research on how to reduce noisy fluctuations in a time series and improve the overall quality of MODIS LAI product. Additionally, some methods suffer from high computational costs and difficulties in operational implementation, challenging their application to regional or global scales. Data reanalysis is widely used in meteorology, but there are few reports on remote sensing reanalysis products. MODIS LAI has a clear theoretical basis and offers a long time series (2000 to present). Therefore, it is an optimal choice to reanalysis based on the principles of high computational efficiency, easy adaptation to process changes, and reasonable accuracy to improve their overall quality. In this way, data consistency can be ensured without changing the advantages of the existing products (the physics-based LAI generation process).

This study proposes a spatiotemporal information composition algorithm (STICA) to directly introduce prior

TABLE I
SITE INFORMATION FOR GBOV. LAND COVER DATA FROM THE MCD12Q1 IN 2018

Site Name	Site Id	Dominant Land Cover (3 km × 3 km)	Latitude	Longitude
Bartlett Experimental Forest	BART	Forest	44.0639	-71.2873
Blandy Experimental Farm	BLAN	Crops & Savannas	39.0603	-78.0716
Central Plains Experimental Range	CPER	Crops	40.8155	-104.7457
Dead Lake	DELA	Forest & Savannas	32.5417	-87.8039
Disney Wilderness Preserve	DSNY	Crops & Savannas	28.1250	-81.4363
Guanica Forest	GUAN	Crops & Savannas	17.9695	-66.8687
Harvard Forest	HARV	Forest	42.5378	-72.1715
Jones Ecological Research Center	JERC	Crops & Savannas	31.1948	-84.4688
Jornada	JORN	Crops	32.5907	-106.8426
Konza	KONA	Crops	39.1104	-96.6129
Lajas	LAJA	Crops & Savannas	18.0213	-67.0769
Moab	MOAB	Crops	38.2484	-109.3883
Niwot Ridge Mountain Research Station	NIWO	Crops & Savannas	40.0543	-105.5825
Onaqui	ONAQ	Crops	40.1776	-112.4524
Oak Ridge	ORNL	Forest & Savannas	35.9641	-84.2826
Ordway-Swisher Biological Station	OSBS	Forest & Savannas	29.6762	-82.00847
Smithsonian Conservation Biology Institute	SCBI	Forest	38.8929	-78.1395
Smithsonian Environmental Research Center	SERC	Forest & Savannas	38.8902	-76.5601
Santa Rita	SRER	Crops	31.9107	-110.8355
Steigerwaldt Land Services	STEI	Forest & Savannas	45.5089	-89.5864
North Sterling	STER	Crops	40.4619	-103.0293
Talladega National Forest	TALL	Forest	32.9505	-87.3933
UNDERC	UNDE	Forest & Savannas	46.2340	-89.5375
Woodworth	WOOD	Crops	47.1282	-99.2414

spatiotemporal correlation information and multiple quality assessment (MQA) information into the existing MODIS LAI product. The primary objective of this study is to propose the STICA and evaluate its performance through direct validation with ground reference and evaluation based on simulated time series, performance in different biome types, and specific regional scales. We hope to apply STICA to derive a MODIS LAI reanalyzed product in the next step.

The structure of this article is organized as follows. Section II provides a framework for the proposed STICA and describes the datasets and evaluation metrics used in this study. Section III details the evaluation of the performance of the tile scale obtained by STICA. We discuss the parameter sensitivity, key points of improvement, advantages of multiple information, and prospects of STICA in Section IV. Concluding remarks are provided in Section V.

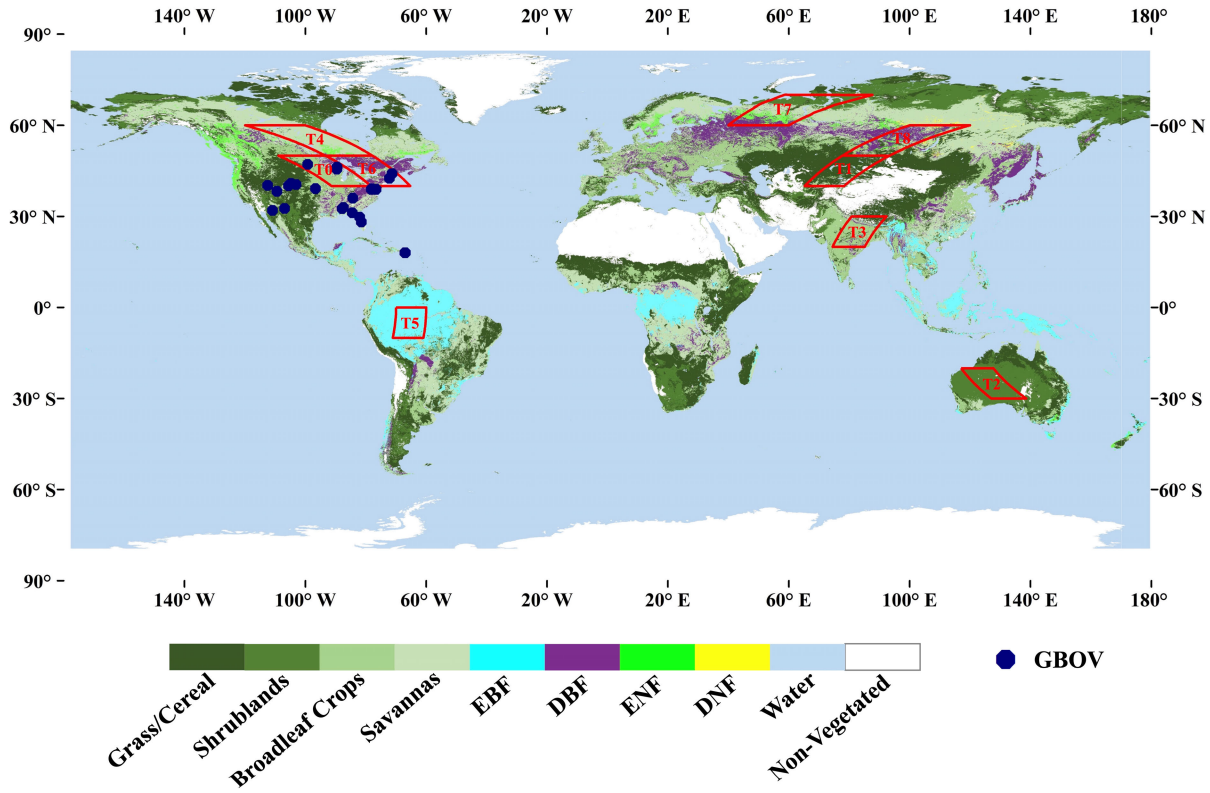

Fig. 1. Geographical distribution of the selected GBOV sites and the specific study area. The background color indicates the biome types from the 2018 MCD12Q1 classification scheme. The blue dots represent the GBOV sites, and the red boxes show the tiles selected for analysis in this study: T0 = h11v04, T1 = h23v04, T2 = h29v11, T3 = h25v06, T4 = h12v03, T5 = h11v09, T6 = h12v04, T7 = h20v02, and T8 = h23v03.

II. Materials and Methodology

A. Datasets

1) MODIS Land Cover Map: The biome classification map is an auxiliary dataset of MODIS LAI and is used to reduce the uncertainty of the retrieval algorithm. An accurate biome classification map is essential for linking satellite observations with surface parameters. We used the biome classification map to identify the same type of pixels and include them in the algorithm calculation. The MODIS land cover product (MCD12Q1) supplies global maps at 500-m spatial resolution and annual time steps. The product was created using a supervised classification of spectral–temporal features [56] and contains 13 science datasets. The MCD12Q1 used the LAI legacy classification scheme, i.e., B1: grasses and cereal crops; B2: shrubs; B3: broadleaf crops; B4: savannas; B5: evergreen broadleaf forests (EBF); B6: deciduous broadleaf forests (DBF); B7: evergreen needleleaf forests (ENF); and B8: deciduous needleleaf forests (DNF) [19], [56]. Fig. 1 displays the approximate global biome-type distribution based on the 2018 land cover.

2) MODIS LAI Product: The MODIS LAI algorithm retrieves LAI using a lookup table (LUT) inversion strategy based on the theory of 3-D radiative transfer and stochastic radiative transfer theory [2], [3]. The operational algorithms include the main algorithm and the backup algorithm, which are based on the radiative transfer equation and the empirical relationship between canopy LAI and normalized vegetation index (NDVI), respectively [10], [57], [58]. The mean values of LAI, FPAR, and their dispersions, standard deviation of LAI (STD LAI) and STD FPAR, are reported as retrievals and their uncertainties [2], [3]. Corresponding quality information is also stored in the layer [20]. Users should consult the quality flags when using these products [19].

The standard collection 6 MODIS LAI/FPAR product suite (MOD15A2H) is provided at a 500-m spatial resolution and eight-day temporal resolution [59], covering the period from 2002 to the present and having global coverage. In general, 46 composites are produced per year, but composites may be lost due to the influence of the sensor or other factors. This product is projected on a sinusoidal grid and distributed as standard hierarchical data format (HDF) files. Each file contains six scientific layers: 1) FPAR; 2) LAI; 3) FparLai_QC; 4) FparExtra_QC; 5) FparStdDev; and 6) LaiStdDev. We used the LAI, LaiStdDev, and FparLai_QC layers, which store the LAI retrieval, the retrieval uncertainty, and the quality control information, respectively [2], [19], [60]. The year 2018 over selected tiles was used in this study.

3) Ground LAI Reference: There is an increasing emphasis on quantifying product accuracy based on in situ reference measurements with the growing availability of Earth observation products [61], [62]. We evaluated the performance of STICA LAI against the Copernicus Ground-Based Observations for Validation (GBOV) LAI, as the GBOV database is regularly updated with consistent products and has enough data for evaluation within a year. The GBOV service is part

TABLE II
PERCENTAGE OF BIOME TYPE IN THE SIMULATED LAI

Biome Type	Percentage (%)
Grasslands	25.41
Broadleaf Croplands	6.54
Savannas	42.91
Deciduous Broadleaf Forests	22.20
Evergreen Needleleaf Forests	0.11
Deciduous Needleleaf Forests	0.04

of the Copernicus Global Land Service (CGLS) and aims to develop and distribute robust in situ datasets from this selection of ground-based monitoring sites for quantitative and systematic validation of land products [61]. A GBOV reference measurement database has been created by quality control and reprocessing raw measurements from existing in situ sites. The established database contains top of canopy reflectance, surface albedo, LAI, FPAR, the fraction of covered ground, soil moisture at 5 cm depth, and land surface temperature. These data are freely available to the community via the GBOV portal (https://gbov.acri.fr).

We selected the GBOV LAI measurements of 2018 as a reference, with a total of 24 sites (Table I and Fig. 1). A square area of 3 × 3 km centered on the site location was selected as the study area, and the MODIS LAI product corresponding to the site was 6 × 6 pixels. Only valid pixels were calculated in the 3 × 3 km area to improve the credibility of the ground LAI. The criteria for valid pixels are that effective pixels used in aggregation value are greater than 80% and the input and output of the land product value of the data aggregation process are within the range. After filtering, there were 21 available sites (307 measurements) to be used for validation [61], [62], among which JORN, MOAB, and Central Plains Experimental Range (CPER) sites were not used for verification because there was no available data after filtering.

4) Simulated LAI Time Series: Uncertainty analysis for validating remote sensing products based on ground measurement data is a direct detection method with pixels as the basic unit, which can directly verify the quality of remote sensing products. However, this verification method is limited by spatial scale and resources. Using simulated data allows us to explore the behavior of the algorithm by stripping away sources of uncertainty and adding arbitrary uncertainty to evaluate its advantages and limitations. In this study, we generated a reference dataset region to better understand the performance of STICA. We add random uncertainties to the simulated data to compare the improvement effect of STICA under different uncertainty ranges. The simulated LAI time series were generated based on an area (tile: h11v04, size: 500 × 500 pixels) of raw MODIS LAI covering six biome types (Table II). The approach is described in detail in the following.

a) Standard LAI time series: We first averaged the main algorithm retrievals of 46 composites to obtain the annual mean curves of 2018 for different biome types. These curves were accompanied by jitter caused by sensor failures or observation conditions. The SG filter approach fits a curve with a local polynomial function, which can capture rapid and subtle changes in the time series [32]. Hence, we applied the SG filter to correct the annual mean curves to obtain smooth annual curves for different biome types. We refer to these smooth annual curves as ancillary LAI.

Based on auxiliary LAI, the standard LAI time-series generation steps are as follows. First, we replaced the backup algorithm retrievals with the auxiliary LAI of the same biome type and kept the main algorithm retrievals constant. Second, we applied the SG filter to smooth each pixel. Finally, the smooth LAI curve represented the simulated standard LAI time series for one year.

b) Simulated uncertainty-added (SUA) LAI time series: To obtain the SUA LAI time series, random uncertainty was added to each pixel of the standard LAI time series, with a normal distribution. The range of uncertainty varied between plus and minus 40%. We divided the relative uncertainties into four categories to obtain a quality classification of the SUA LAI time series, as shown in Table III.

TABLE III
RELATIVE UNCERTAINTY CORRESPONDING TO THE MQA AND QUALITY CLASSIFICATION

Relative Uncertainty (R_U, percentage)	MQA	Quality Classification
$0 < R\_U \leq 10$	8	Good
$10 < R\_U \leq 20$	6	Moderate
$20 < R\_U \leq 30$	4	Moderate
$R\_U > 30$	2	Poor

Finally, a total of four simulated datasets were generated as follows: 1) standard LAI time series; 2) land cover map; 3) SUA LAI time series; and 4) MQA. In this study, the land cover was introduced to distinguish the biome types of pixels and control the pixels involved in the calculation; MQA is an index that assigns various weights to pixels by employing spatiotemporal correlation information; SUA LAI time series were the input data in STICA; and standard LAI time series were used to evaluate the quality improvement effect.

B. Proposed STICA

The workflow of STICA (Fig. 2) includes four main steps. The details are described in Sections II-B1–II-B4.

1) Step 1: MQA: Although STICA is related to LAI information at neighbor periods/locations, this information carries varying levels of uncertainty. Our algorithm comprehensively determined this uncertainty using multiple indicators, called MQA [Fig. 3(d)]. Among them, the algorithm path (AP) [Fig. 3(a)] is an essential quality indicator, and many research analyses demonstrate that the main algorithm provides the highest quality and precision retrievals [19], [63]. The estimated retrieval uncertainty, STD LAI [Fig. 3(b)], is only generated when the main algorithm is used [2], [3], [60]. Time-series stability [TSS, Fig. 3(c)] represents the fluctuation of a time series, with high values implying more jitter [64]. The

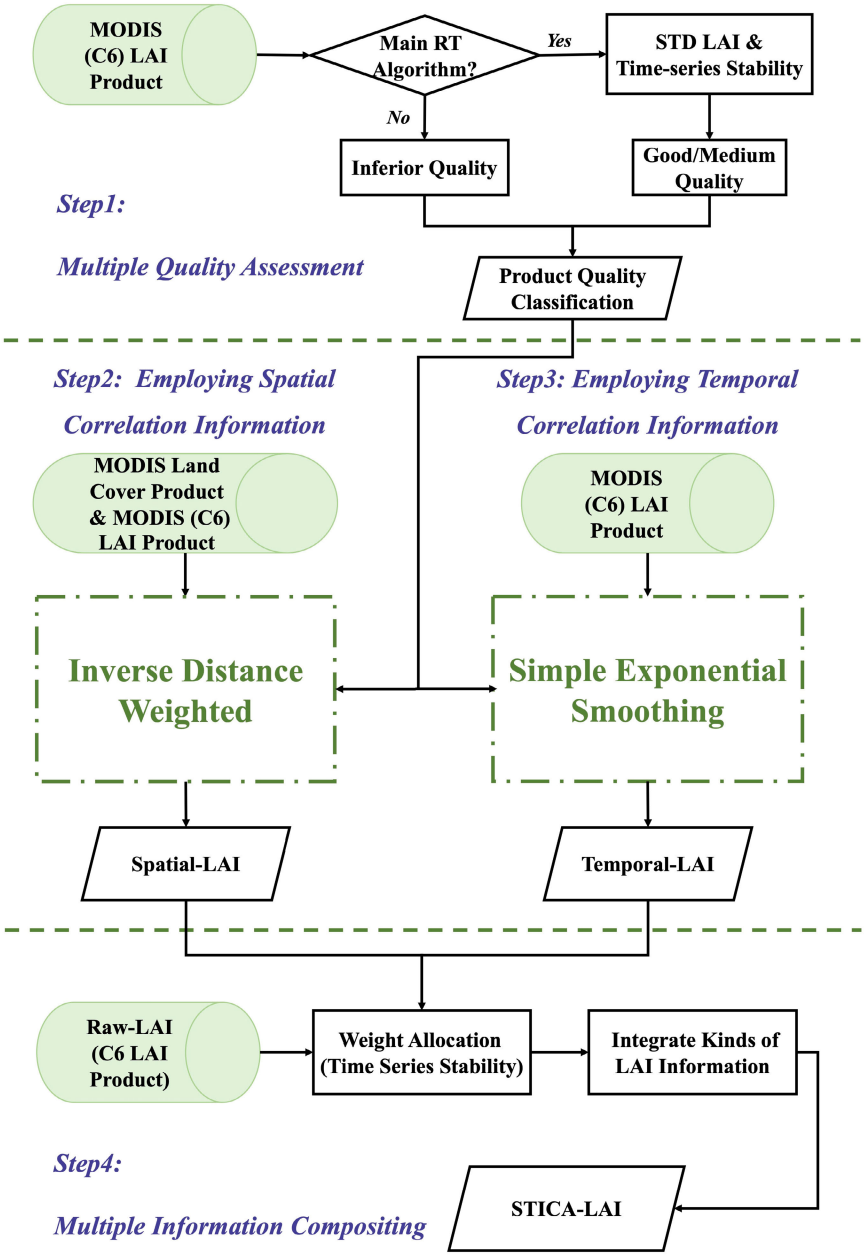

Fig. 2. Workflow of the proposed STICA.

equation and details of the TSS are provided in the Appendix. The AP and STD LAI are archived in the quality assurance (QA) layers associated with the MODIS product. To calibrate the proportion of the main algorithm and backup algorithm, we selected eight GBOV sites (Bartlett Experimental Forest (BART), Harvard Forest (HARV), Smithsonian Conservation Biology Institute (SCBI), Talladega National Forest (TALL), KONA, ONAQ, SRER, and WOOD) with uniform vegetation types and evaluated the performance using root-mean-square error (RMSE) as the evaluation index (Table IV). The weight ratio of the backup and the main algorithm was set as 4:6. We then mapped STD LAI and relative TSS (RE-TSS) to the main algorithm retrievals according to the principle that the smaller the value, the greater the weight is. The equation of data mapping of STD LAI and RE-TSS is as follows:

$$y = y_{\max} + \frac{y_{\min} - y_{\max}}{x_{\max} - x_{\min}} \times (x - x_{\min}) \tag{1}$$

where $y_{\max}$ and $y_{\min}$ are the maximum and minimum values of the mapping target interval with 0.5 and 0, respectively. $x_{\max}$ and $x_{\min}$ are the maximum and minimum values of data (STD LAI or RE-TSS), respectively. x is the data value (STD LAI or RE-TSS), and y is the mapping result. Finally, the MQA was obtained by integrating the AP, STD LAI, and RE-TSS.

2) Step 2: Employing Spatial Correlation Information: Inverse distance weighted (IDW) is a commonly used interpolation method in spatial analysis, assuming each location has a local effect. IDW assigns considerable weight to nearby points

TABLE IV
RMSE CORRESPONDING TO THE VALUE OF THE WEIGHT ASSIGNMENT OF THE BACKUP ALGORITHM

Weight Assignment (Backup algorithm: Main algorithm)	1:9	2:8	3:7	4:6	5:5	6:4	7:3	8:2	9:1
RMSE	0.63	0.63	0.61	0.57	0.59	0.62	0.65	0.65	0.67

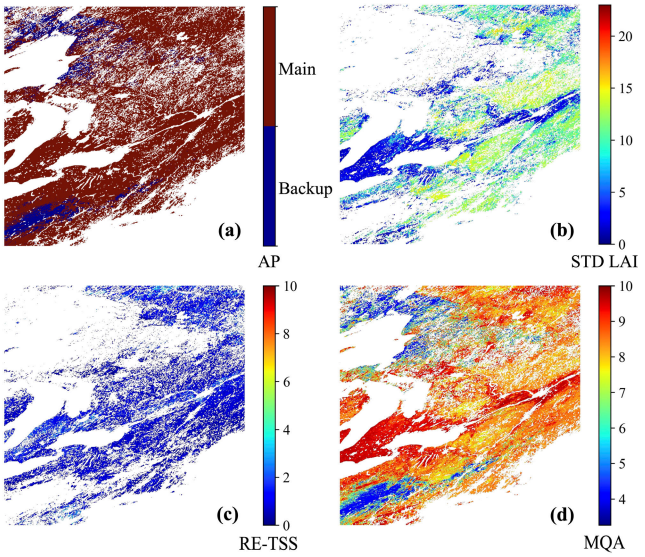

Fig. 3. Spatial distribution of different indicators in tile h12v04-2018265: (a) AP; (b) STD LAI; (c) RE-TSS (formula in the Appendix); and (d) MQA map after the synthesis of multiple indicators.

and reduces it as the distance increases. In our algorithm, we weighted the average of all the eligible pixels within a certain spatial range of the target pixel, with eligibility determined by the same land cover type. A neighboring pixel with a higher MQA value contributed more to the target pixel. The spatial LAI is calculated as

$$S\_\mathrm{LAI}_{(x,y)} = \frac{\sum_{i=1}^{n} \mathrm{Raw\_LAI}_i \times D_i \times \mathrm{MQA}_i}{\sum_{i=1}^{n} D_i \times \mathrm{MQA}_i} \tag{2}$$

where n is the number of pixels of the same land cover in the window around the target pixel. Spatial LAI remains unchanged when there is no same land cover type in the window. D_i represents the inverse of the spatial Euclidean distance (between candidate and target pixel), defined as

$$D_i = \mathrm{ED}_i^{-\alpha} \tag{3}$$

$$\mathrm{ED}_i = \sqrt{(x - x_i)^2 + (y - y_i)^2} \tag{4}$$

where α is a positive power exponent that controls the decay rate of a candidate pixel weight, and the weight of distant candidate pixels decreases rapidly with the increase of α. It is necessary to evaluate the optimal power exponent α and the window size, which ensures the overall utility. We randomly selected an area (200 × 200 pixels) in the simulated LAI time series and obtained RMSE by varying parameters to investigate the two parameters.

3) Step 3: Employing Temporal Correlation Information: Simple exponential smoothing (SES) is frequently used as an exponential MA model in the time-series domain due to its simplicity, computational efficiency, adaptability to processing changes, and reasonable accuracy [65], [66]. It is an intuitive prediction method with unequal weights for time series [67], giving the heaviest weight to recent observations and a smaller weight to those to a distant time. While traditional SES uses only the predecessors of the target timestamp as input, we referenced the approach of Yi et al. [68] and incorporated both predecessors and successors of the target timestamp.

Similar to spatial LAI, we weighted the average of all the eligible pixels of the target pixel within a certain temporal period. More weight was given to pixels that are temporally closest to the target pixel and have higher MQA values. The temporal LAI can be expressed as

$$T\_\mathrm{LAI}_{(x,y)} = \frac{\sum_{j=1}^{m} \mathrm{Raw\_LAI}_j \times E_j \times \mathrm{MQA}_j}{\sum_{j=1}^{m} E_j \times \mathrm{MQA}_j} \tag{5}$$

where m represents the length of the time series participating in calculating target pixels. E_j is defined as follows:

$$E_j = \beta \times (1 - \beta)^{j-1} \tag{6}$$

where j is the time interval between a candidate pixel and a target pixel, and β denotes the rate at which the weight changes over time. The smaller β represents the slighter decrease of weight over the time interval. Similarly, we used the same simulated LAI time series to determine the two parameters of the length of the time series m and smoothing parameter β.

4) Step 4: Multiple Information Compositing: STICA integrated spatial and temporal LAI as well as raw MODIS LAI. Different weights were assigned to the LAI of the three kinds of information to obtain the final LAI (STICA LAI)

$$\mathrm{STICA}_{\mathrm{LAI}(x,y)} = \frac{S\_\mathrm{LAI}_{(x,y)} \times W1 + \mathrm{T\_LAI}_{(x,y)} \times W2 + \mathrm{Raw\_LAI}_{(x,y)} \times W3}{W1 + W2 + W3} \tag{7}$$

where $W1$, $W2$, and $W3$ represent the weights of spatial, temporal, and raw LAI, respectively, which can be expressed as follows:

$$W_k = \frac{1}{\text{relative } \mathrm{TSS}_k(x, y)}, \quad k = (1, 2, 3) \tag{8}$$

where relative $\mathrm{TSS}_k(x, y)$ represents the fluctuation of the time series at pixel (x, y). TSS is used to quantify the LAI stability of three types of information. High values imply a

poor TSS of data; conversely, low values indicate a stable time-series performance of data [64]. The STICA LAI was only obtained from the average of spatial LAI and temporal LAI when the target was the starting or ending time, as TSS required at least one data period before and after the target pixel.

The final output LAI layers included the raw MODIS LAI, the spatial LAI, the temporal LAI, and the STICA LAI. The output quality layers contained the raw QA layers, the MQA layers, and the absolute difference (AD) of LAI between STICA LAI and the raw MODIS LAI.

C. Study Area

In the algorithm evaluation with ground LAI reference, we selected 21 sites (Fig. 1 and Table I), which covered a variety of biome types: forests (including EBF, ENF, DBF, and broadleaf needleleaf forests), crops (including grasslands, shrublands, and broadleaf croplands), and savannas. In addition, we selected eight tiles (2400 × 2400 pixels per tile) dominated by a single biome as representatives of different biome types: h23v04 (coverage of B1: 84.27%), h29v11 (B2: 97.63%), h25v06 (B3: 33.00%), h12v03 (B4: 76.39%), h11v09 (B5: 94.01%), h12v04 (B6: 33.84%), h20v02 (B7: 31.09%), and h23v03 (B8: 12.95%) to observe the annual LAI curve fluctuations over different biomes types and evaluate the performance of the algorithm under a specific biome type. Fig. 1 shows the geographic locations and coverage of eight tiles with the highest percentage of distinct biomes globally; we only analyzed pixels corresponding to those biome types.

The Amazon forest plays a crucial role in the hydrologic cycle [69], which is critical to balancing the global carbon budget and improving climate projections [70]. However, high cloud cover and aerosol concentration affect this region throughout the year, leading to reduced-quality observation data for optical sensors and hindering LAI retrievals [71], [72]. Consequently, evaluating the performance of STICA over the Amazon forest region was crucial. To achieve this, we selected the h11v09 tile (2400 × 2400 pixels) centered on the Amazon forest (Fig. 1) in 2018 and compared the TSS and time-series anomaly (TSA) of STICA with the raw MODIS LAI. Additionally, we used a local area (500 × 500 pixels) with a proportion of EBF exceeding 97% in h11v09 to compare the LAI changes in two adjacent periods and evaluate the performance of STICA and raw LAI indirectly. To assess their performance, we set the MODIS LAI value on day of year (DOY) of 201 in 2018 (D1) as the standard LAI and subtracted D1 from the raw and STICA LAI values on DOY 209 in 2018 (D2) to obtain the difference of raw LAI and STICA LAI, which were then compared.

D. Quantitative Evaluation Metrics

Accuracy and uncertainty evaluation indices were used to evaluate the performance of the algorithm. The first was the RMSE, defined as

$$\mathrm{RMSE} = \sqrt{\frac{1}{n}\sum_{i=1}^{n}\left(\mathrm{LAI}_{(x,y)} - \mathrm{STICA\_LAI}_{(x,y)}\right)^2} \tag{9}$$

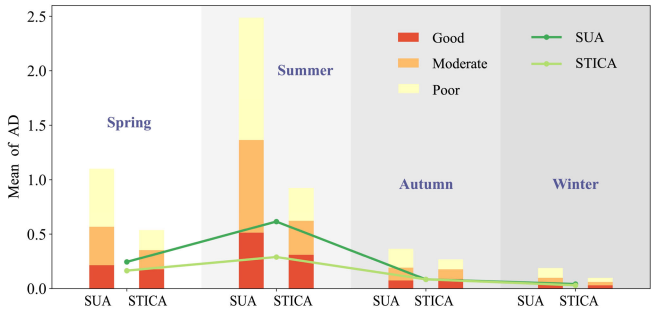

Fig. 4. Bar plot comparing SUA LAI with STICA LAI. From left to right are spring, summer, autumn, and winter. The solid lines denote the mean of AD with different seasons. Red, orange, and yellow represent the quality classification with good (MQA = 8), moderate (4 ≤ MQA ≤ 6), and poor (MQA = 2), respectively.

where $\mathrm{LAI}_{(x,y)}$ represents SUA LAI or raw MODIS LAI.

The recently proposed time-series metrics TSS is defined as the distance from the value at the target moment to the linear interpolation line; the linear interpolation line can be calculated by the data at the former and latter time series of the target moment date to quantify the fluctuation of a time series [64]. In this study, we compared the cumulative TSS by adding up all the TSS within a year.

Another quantitative evaluation metric is the standardized anomaly (SA), which can quantify the TSA to show the trends of different variables [58]. It is calculated as follows:

$$\mathrm{SA}(t) = \frac{X(t) - \mathrm{mean\_}t(X(t))}{\mathrm{Std\_}t(X(t))} \tag{10}$$

where X and t represent the variable time series for one year and the time, respectively; mean_t and Std_t indicate the average and STD metrics calculated from the time dimension, respectively. TSA is the sum of pixels number greater than the threshold value per year in the region [64]. We used a threshold value greater than 1, as follows:

$$\mathrm{TSA} = \mathrm{sum}(|\mathrm{SA}| \geq 1). \tag{11}$$

In this study, density represents the proportion of different values in the statistics. The density here is related to the bins setting of the drawing container but does not change the statistical significance. In addition, the AD of LAI is also utilized to quantify the differences between STICA and raw LAI; AD is expressed as

$$\mathrm{AD}_{(x,y)} = |\mathrm{LAI}_{(x,y)} - \mathrm{STICA\_LAI}_{(x,y)}| \tag{12}$$

where $\mathrm{LAI}_{(x,y)}$ represents SUA LAI or raw MODIS LAI.

III. Results

A. Evaluation Based on Simulated Datasets

We compared the mean of AD of the SUA and STICA LAI in four seasons with different quality classifications (Fig. 4 and Table V), showing that when the quality classification is poor, the difference in the mean of AD between SUA and STICA is more noticeable. This phenomenon is especially prominent in summer (difference of good: 0.2; moderate: 0.54; and poor: 0.82). The improvement of STICA is more evident with the decreasing trend in data quality. The mean of AD in summer

TABLE V
MEAN OF AD OF SUA LAI AND STICA LAI AND THEIR DIFFERENT VALUES WITH DIFFERENT QUALITY CLASSIFICATIONS

Seasons	MQA	SUA	STICA	Difference
Spring	Good	0.21	0.18	0.03
	Moderate	0.35	0.18	0.17
	Poor	0.53	0.18	0.35
Summer	Good	0.51	0.31	0.2
	Moderate	0.85	0.31	0.54
	Poor	1.12	0.30	0.82
Autumn	Good	0.07	0.09	-0.02
	Moderate	0.12	0.09	0.03
	Poor	0.17	0.09	0.08
Winter	Good	0.04	0.03	0.01
	Moderate	0.06	0.03	0.03
	Poor	0.09	0.04	0.05

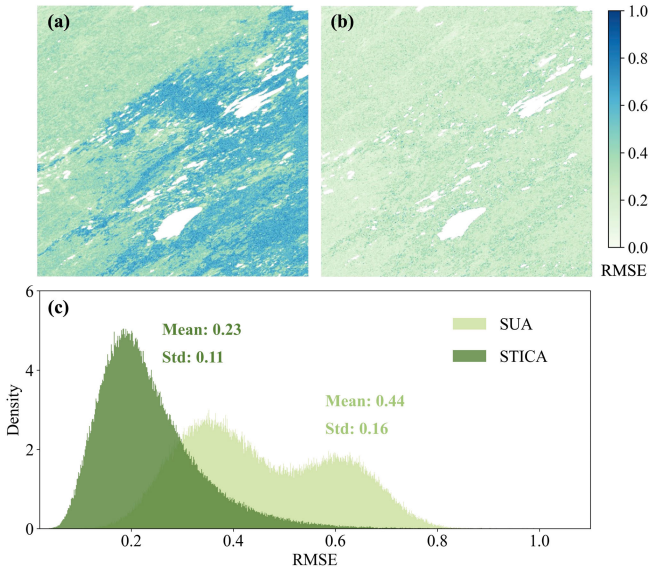

Fig. 5. Spatial distributions of RMSE from: (a) SUA and (b) STICA LAI. The color bars represent the RMSE from small (light) to large (dark). (c) Comparison of the density distribution of RMSE between SUA (light green) and STICA (dark green).

and winter is the maximum and minimum, which may result from the highest and lowest LAI in these two seasons. STICA (light green solid line) is always below the SUA (dark green solid line), showing that STICA performs better than SUA LAI in each season.

We also compared the spatial distribution of RMSE between SUA [Fig. 5(a)] and STICA [Fig. 5(b)] LAI. The panel indicates that STICA exhibits a smaller RMSE, and more dark color pixels are displayed in the spatial distributions of SUA. The RMSE of STICA is concentrated in smaller numbers (mean = 0.23) than SUA (mean = 0.44) [Fig. 5(c)]. These indicate that STICA can improve low-quality retrievals and reduce uncertainties.

B. Validation Using GBOV LAI Reference

STICA outperforms raw LAI in comparison to ground observations. From raw [Fig. 6(a)] to STICA [Fig. 6(b)], the R^2 increased from 0.79 to 0.81, the RMSE decreased from 0.81 to 0.68, and a decrease in relative RMSE (RRMSE) is from 30.07% to 25.51%, resulting in a 16% improvement in overall accuracy. Furthermore, we observed an increase in bias from −0.24 to −0.06, which can be attributed to the overestimation of some raw LAI, an issue that STICA mitigated. Notably, STICA is remarkably effective at correcting extreme outliers [circled in red in Fig. 6(a)]. In view of biome types, there was a noticeable improvement for the pure forests type (red), with RMSE decreasing from 1.06 to 0.62 and R^2 increasing from 0.6 to 0.8 [Fig. 6(c)]. Pure crops (blue) show similar improvements, with a 0.07 decrease in RMSE and a 0.01 increase in R^2. There was only a slight increase/decrease in RMSE/R^2 of the hybrid type. From the perspective of the quality classification [Fig. 6(d)], STICA performed better in all quality levels than the raw LAI. When the quality classification was poor, R^2 increased from 0.53 to 0.90 (increasing 70%), and RMSE reduced from 1.43 to 0.60 (decreasing 58%); for medium quality, RMSE decreased by 0.1 and R^2 increased by 0.04; and for good quality, R^2 and RMSE changed only slightly. Similar conclusions can be drawn from algorithmic evaluations of simulated LAI time series (Fig. 4). In general, STICA effectively improved the quality of LAI by combining prior spatiotemporal correlation information and MQA information.

The difference distribution range of the remaining 21 sites after data filtering is shown in Fig. 7. The RMSE of STICA is smaller than that of raw LAI for all GBOV sites, except for Dead Lake (DELA), Ordway-Swisher Biological Station (OSBS), Smithsonian Environmental Research Center (SERC), Disney Wilderness Preserve (DSNY), and Jones Ecological Research Center (JERC). The distribution of the

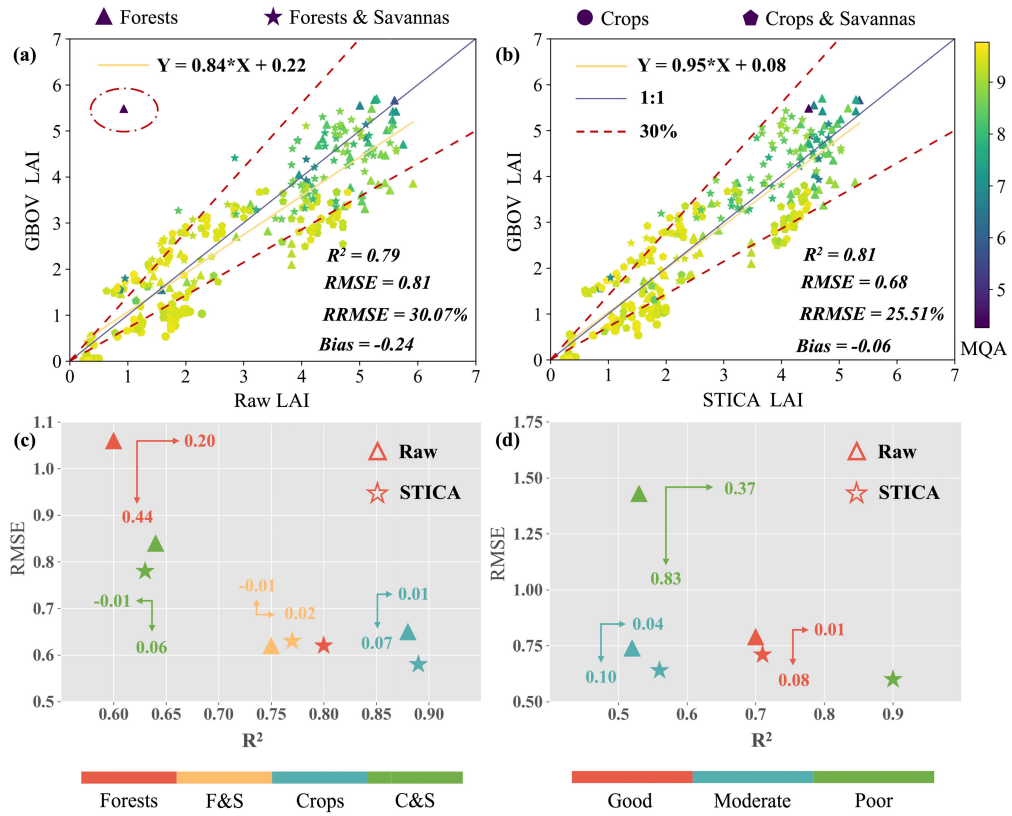

Fig. 6. Scatterplots comparing: (a) raw LAI and (b) STICA LAI with GBOV LAI reference (21 sites and 307 measurements). Symbol colors correspond to MQA from 4 (poor) to 10 (good), and the shape of characters represents different biome types. (c) and (d) compare the RMSE and R^2 between raw and STICA LAI within different biome types (F&S: forest and savannas and C&S: crops and savannas) and quality classification (good: MQA $\geq$ 9; moderate: 7 $\leq$ MQA $<$ 9; and poor: MQA $<$ 7), respectively. The left and right arrows represent the change of STICA compared to raw LAI (the right means increasing, and the left means decreasing) in R^2, and the top and bottom arrows indicate the change of STICA compared to raw LAI (the bottom means reducing, and the top means increasing) in RMSE. The length of the arrow corresponds to the shift (the longer the arrow, the more changes are remarkable). The numbers denote the specific changes in value.

difference for raw is extensive, whereas for STICA, the difference of STICA LAI is distributed around zero and the most significant quality improvement is observed at SCBI (RMSE difference: 0.89), HARV (0.34), TALL (0.30), and UNDE (0.22). Of these sites, three are pure forests type, and only the UNDE site is a hybrid biome. Notably, STICA effectively corrects large abnormal values at the SCBI sites and exhibits similar improvements at HARV, ORNL, Blandy Experimental Farm (BLAN), and Guanica Forest (GUAN) sites. While the distribution range of the difference and RMSE of crops shows minimal enhancement due to the small LAI values, STICA performs better for pure biome than hybrid biomes. To conclude, STICA demonstrates higher accuracy compared to raw LAI.

C. Performance Over Different Biome Types

The ideal LAI curve increases and decreases monotonically with the change of seasons. However, the LAI curves jitter mainly due to poor atmospheric conditions, sensor hardware issues, or other technical problems [73]. The uncertainty of the MODIS LAI time series originates from the large differences in the observed conditions of two adjacent time windows, resulting in a relatively poor temporal consistency. STICA reduces noisy fluctuations, and the generated curves agree more with the expected phenological pattern than raw LAI (Fig. 8). Among biomes, EBF has the greatest fluctuation, resulting in the most improvement from STICA. The same conclusions are also derived from the approximate range of TSS (Fig. 9). STICA effectively reduces the STD and better captures the trajectory of LAI.

We used the TSS metric indicating temporal stability to quantitatively assess the eight biome types (Fig. 9). STICA showed similar variations with a shorter approximate range of TSS and a significant reduction in average TSS, demonstrating the improvement of STICA over raw LAI. Among all types, EBF and shrublands showed a significant improvement, with the mean of TSS decreasing from 21.08 to 5.37 (decrease of 74.53%) and from 1.55 to 0.37 (76.13%), respectively. Moreover, the reduction in average TSS from raw to STICA was more than 50% for all biomes. These all indicate that STICA can reduce confounding factors and enhance the temporal stability of LAI among different biome types.

D. Performance Over the Amazon Forest Region

MODIS acquired few high-quality observation data in the Amazon forest region due to the perennial influence of large cloud cover and high-concentration aerosol and saturation of

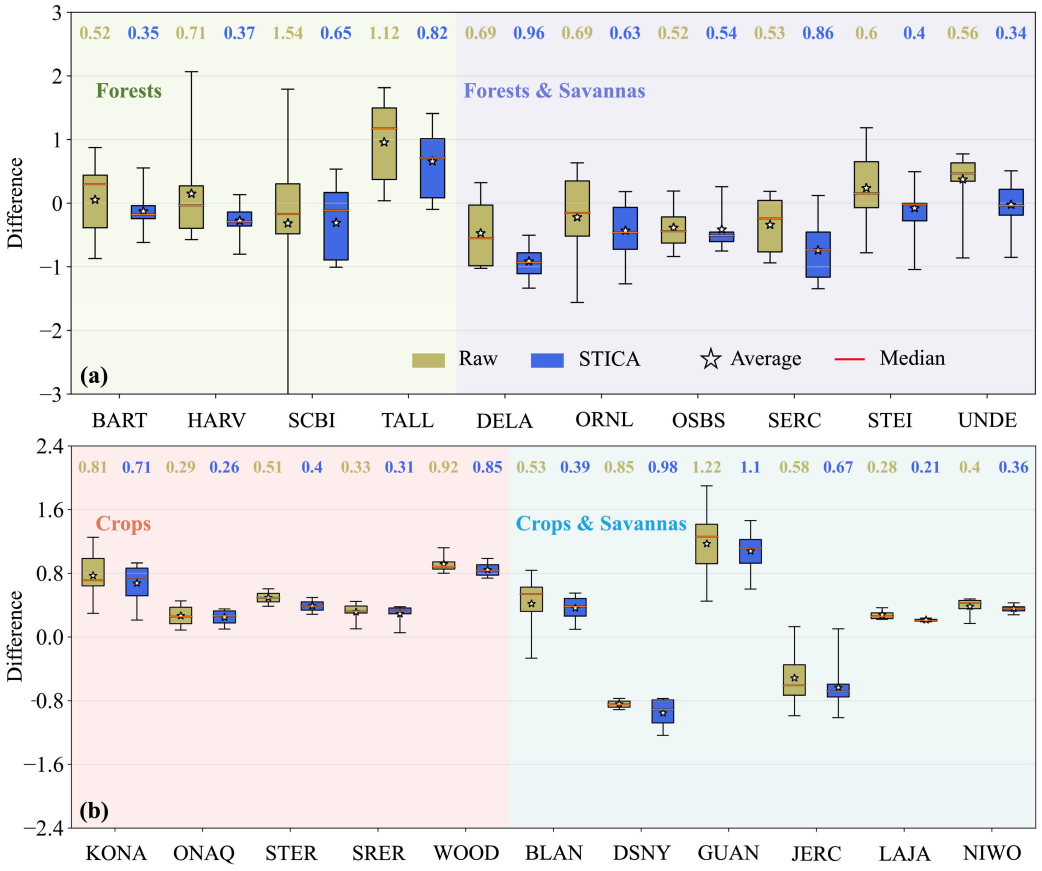

Fig. 7. Accuracy comparison of the difference in LAI at 21 GBOV sites. (a) Distribution of LAI differences for sites corresponding to forests, forest and savannas. (b) corresponds to sites of LAI differences of the biome types crops and crops and savannas. Each site contains a left box (raw) and a right box (STICA). The numbers at the top indicate the RMSE of the raw and STICA LAI, respectively

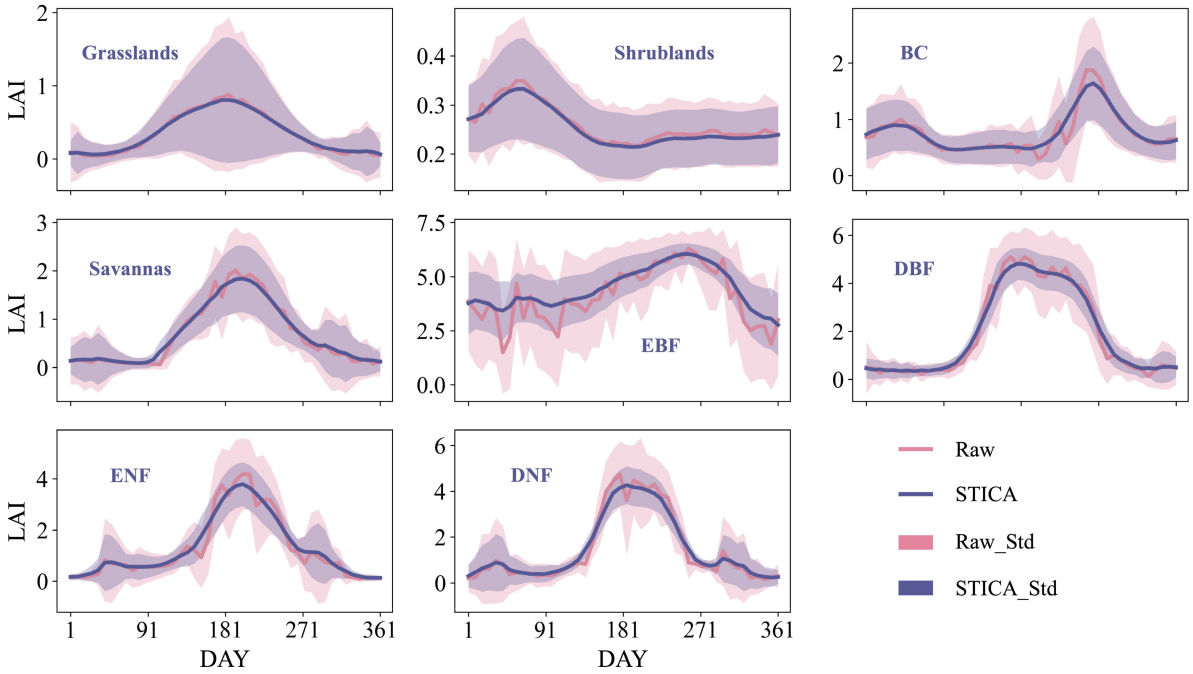

Fig. 8. Temporal comparison of annual curve fluctuations between raw MODIS LAI and STICA LAI over eight biome types. The line and shadow represent the 2018 LAI mean and STD, respectively. Colors correspond to the raw (pink) and STICA (blue) LAI. The eight biome types are grasslands (B1), shrublands (B2), broadleaf crops (BC and B3), savannas (B4), EBF (B5), DBF (B6), ENF (B7), and DNF (B8).

red–NIR, resulting in poor LAI retrieval accuracy. By comparing Fig. 10(a) and (b), it was observed that the spatial distributions of STICA contained more pixels with small TSS, which was also evident in the TSA map [Fig. 10(c) and (d)]

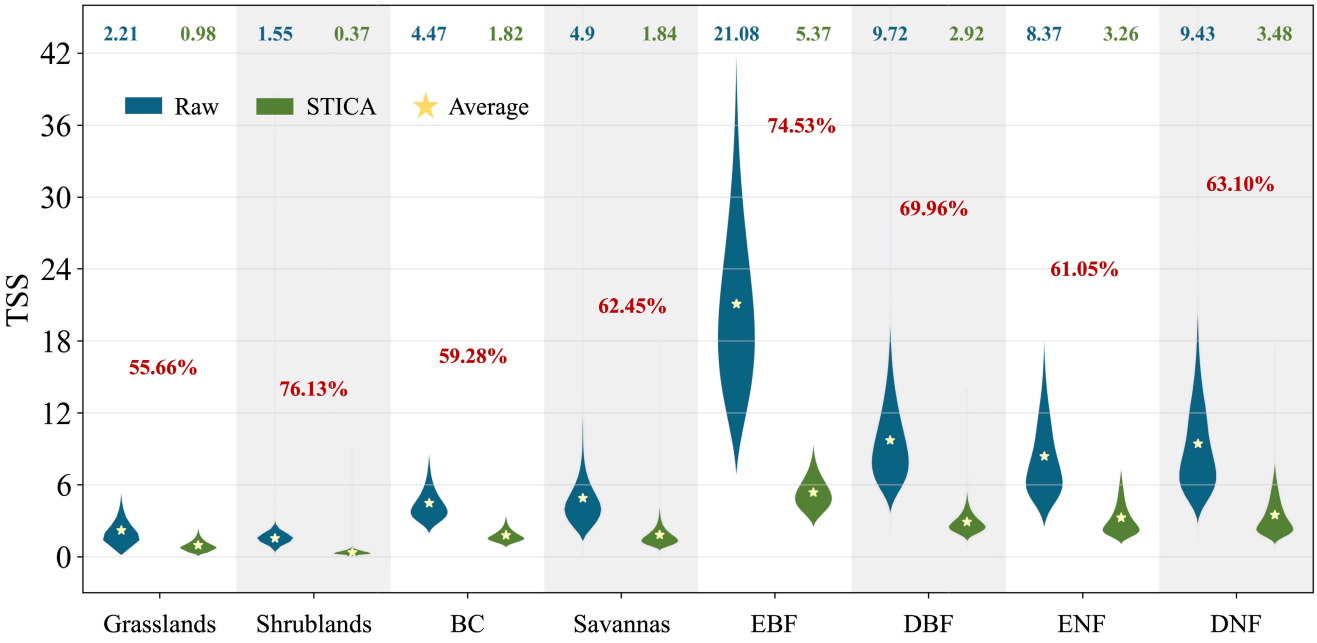

Fig. 9. Comparison of TSS distribution range between raw and STICA LAI over different biome types. Blue and green represent raw and STICA, respectively. Stars indicate the average of the TSS, and the numbers at the top indicate the average of the TSS of raw (blue) and STICA (green). The red numbers are the percent reductions in the mean of TSS from raw to STICA.

where more light-colored areas were predominant in the TSA of STICA. These findings suggest that the overall temporal stability of the spatial pattern of STICA is superior to that of raw LAI. From Fig. 10(e) and (f), the statistics reveal that 99.31% of the total number of pixels in STICA had a TSS less than 10, while the proportion of all pixels with TSA less than 10 improved from 6.34% to 97.57% compared to raw LAI. The mean of TSS decreased from 20.40 to 5.27, and the average of TSA dropped from 14.71 to 3.36, indicating that STICA LAI has a more stable time series with fewer anomalies than the raw LAI.

We also compared that the difference value (DV) of LAI between two adjacent periods in the area dominant biome type is EBF. Theoretically, the LAI of this biome type will not show a significant short-term decline (within 16 days) in summer [74]. Fig. 11(b) and (c) shows that STICA eliminated most abnormally low values, which is more consistent with the expected phenological pattern. Additionally, the negative values of DV coincided with lower MQA. A comparison of the DV percentage [Fig. 11(d)] found that the rate of DV less than -4 (red) for raw was 7%, whereas that for STICA was zero; the rate of DV for raw from -4 to -1 is three times more than that for STICA. Moreover, the DV of STICA (77% of all pixels) in yellow was far more than that of raw (54% of all pixels). Overall, these provide sufficient evidence to denote that STICA can effectively reduce the uncertainty of LAI retrieval caused by low-quality observations.

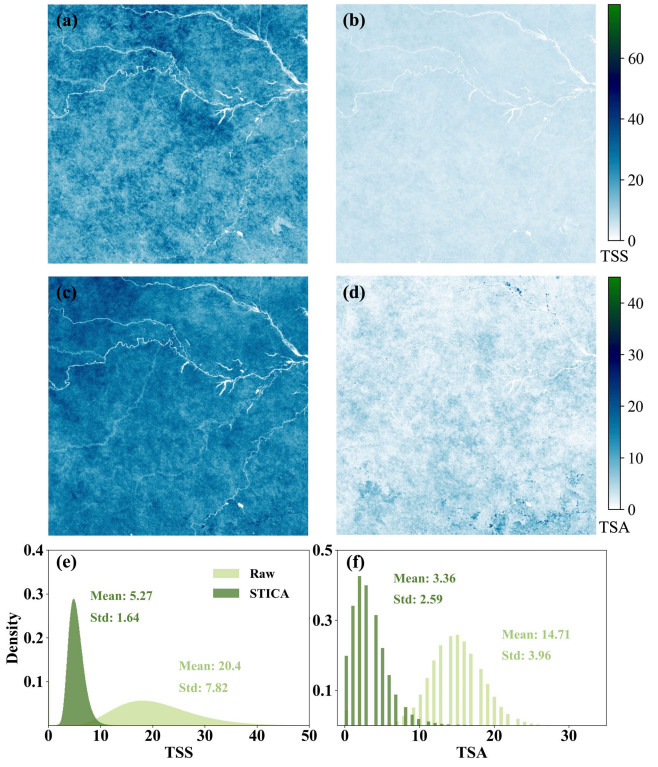

Fig. 10. Spatial distributions of: (a) and (b) TSS and (c) and (d) TSA over the Amazon forest region (h11v09) within 2018. The left and right panels are raw and STICA, respectively. The color bars represent the TSS (TSA) values from small (white) to large (dark green). Comparison of the density distribution of: (e) TSS and (f) TSA over the Amazon forest region. Light and dark green represent the raw and STICA, respectively.

IV. Discussion

Applying STICA significantly improved the LAI quality and reduced the abnormal fluctuations caused by the low-quality retrievals of the raw MODIS LAI. We performed some experiments to explore the optimal algorithm parameter configuration. In the algorithm for employing spatial information, the power exponent α and the half-width of the search window can control the influence of surrounding points on

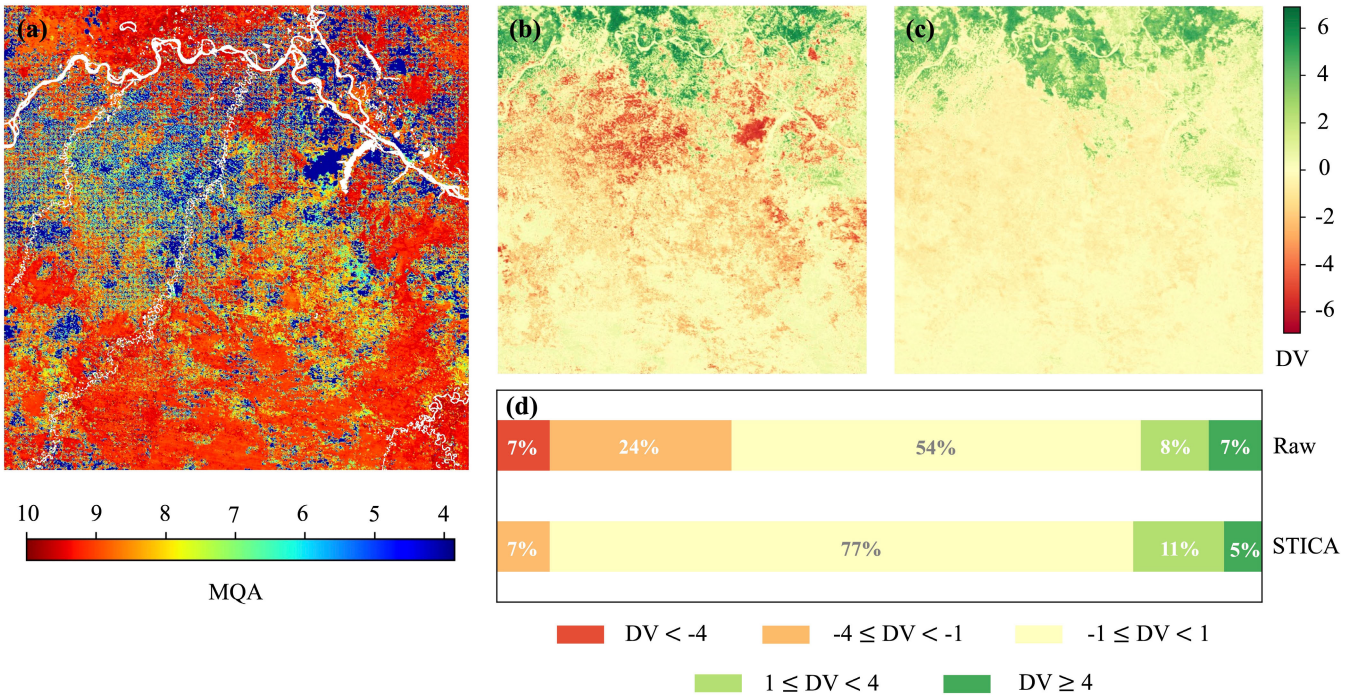

Fig. 11. Comparison of DV of LAI between two adjacent periods: (a) spatial distribution map of MQA on day of year (DOY) of 209 in 2018. The colors correspond to MQA from 4 (poor) to 10 (good). The MODIS LAI value on DOY 201 in 2018 (D1) as the standard LAI; subtracting D1 from raw and STICA LAI values on DOY 209 in 2018 (D2) obtains the DV of: (b) raw and (c) STICA. (d) Proportion of DV of raw and STICA. The top color corresponds to the DV range, and the percentage indicates the proportion of the current color to all pixels.

the interpolated target point and determine the utilization of the spatial information, respectively, and further affect the calculation results. In general, the smaller the half-width of the search window, the stronger the spatial correlation is, but the less spatial information is available. The larger the half-width of the search window, the more the spatial information can be employed, but the weaker the spatial correlation is. A higher power exponent results in less influence from distant points. Therefore, considering the balance between computational efficiency and accuracy, the optimal size of a half-width of the search window and a power exponent can be obtained. Fig. 12 shows the RMSE by varying the power exponent and the half-width of the search window. When the power exponent is equal to two, the gray line is essentially below the other lines. If the power exponent is constant, the RMSE decreases at first and then increases as the half-width of the search window increases. Hence, we determined the power exponent of 2 and the half-width of 4 pixels in our experiments. Similarly, the smoothing parameter of 0.5 and the half-length of 3 were used in the algorithm of employing temporal information (Fig. 13). However, there is only a slight variation in RMSE with the parameter configurations change. Consequently, it can be concluded that the proposed algorithm is not sensitive to parameter selection.

In the algorithm evaluation based on the simulation, only temporal and spatial information was employed during step 4 (i.e., multiple information compositing). The raw LAI information is excluded to avoid errors caused by adding simulation uncertainty to experimental LAI. From the ground-based validation, the low MQA values coincided with high LAI values, which can be explained by the relatively low algorithm accuracy due to signal saturation [14]. Signal saturation is most likely to occur in summer in the presence of lush vegetation, and MODIS LAI retrievals under saturated conditions are overestimated [75]. In both cases, for the simulated-based LAI or ground-based reference, we found that while the quality classification was degrading, the improvement of STICA was more pronounced. STICA can effectively identify and correct most low-quality retrievals. This is consistent with our original intention to keep the continuity with the existing MODIS LAI product. It corresponds well with the raw MODIS LAI retrievals of good quality and enhances the retrievals with poor quality. In addition, we note that the STICA performance of the pure biome is better than that of the hybrid biome, which may be due to the uncertainty in the ground measurements of hybrid pixels as well as the inherent drawback of spatial correlation. The algorithm improvement effect is the most obvious in the pure forest biome. Signal saturation and atmospheric observation conditions lead to LAI retrievals having great uncertainty, limiting the applicability of the raw MODIS LAI for forests with high LAI [75], [76], [77]. However, STICA can alleviate this issue by using spatiotemporal correlation and MQA information. In the Amazon forest region, STICA exhibited greater TSS and effectively reduced anomalies compared with raw LAI. Notably, there was a growth in the spatial distribution of raw LAI, and the same phenomenon occurred in the spatial pattern of STICA, which may have been due to the inherent increase of LAI [74], [78]. Because STICA aims at reducing anomalies and improving the temporal consistency of LAI, it should maintain the temporal pattern of the raw LAI.

Introducing prior knowledge about spatiotemporal correlation information can be done in various ways. We compared

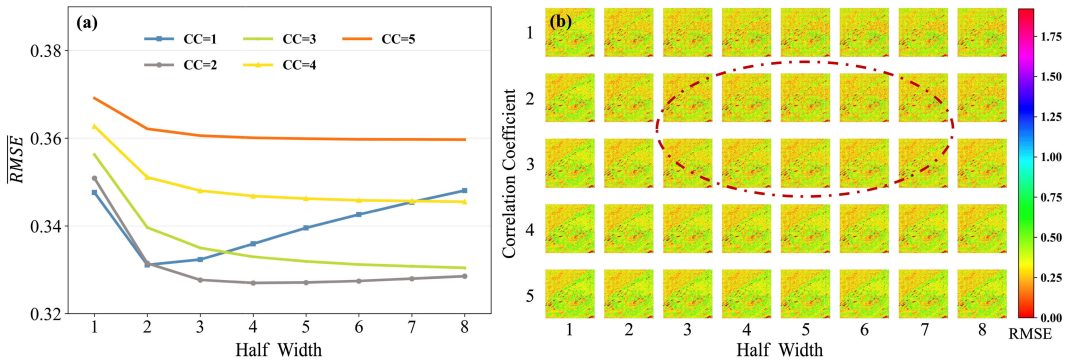

Fig. 12. (a) $\overline{RMSE}$ was calculated from the average of RMSE in the spatial distribution. (b) Spatial distribution of RMSE by changing the correlation coefficient (CC, power exponent α) and the half-width of the search window. The power exponent α controls the weight decay rate of the candidate pixels, and the half-width of the search window is the size of the neighborhood centered on the target pixel. We use power exponent α of 2 as the power exponent and 4 pixels for half-width in the algorithm.

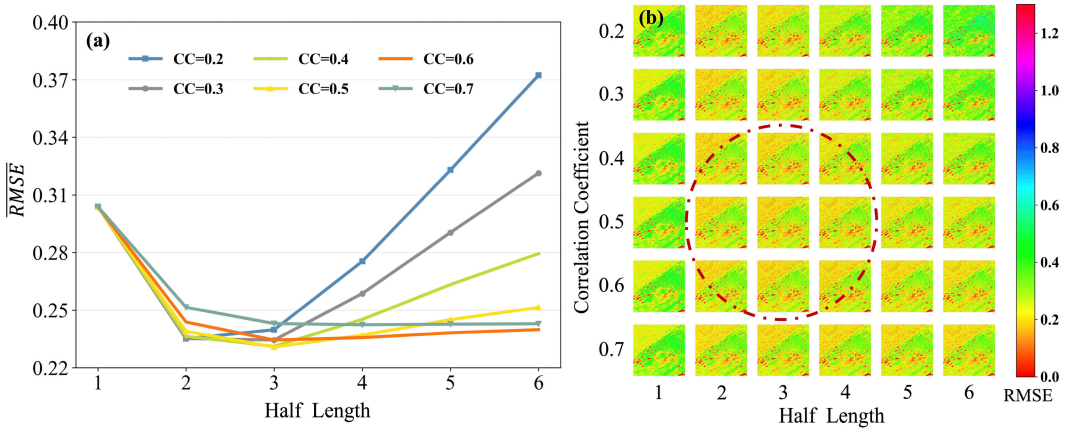

Fig. 13. (a) $\overline{RMSE}$ was calculated from averaging the RMSEs in the spatial distribution. (b) Spatial distribution of RMSE changing the CC (smoothing parameter β) and the half-length of the time series. The smoothing parameter β determines the weight of the candidate pixel, and the half-length denotes the busy period in the computation. We used the smoothing parameter of 0.5 and a half-length of 3.

the utilization of different information based on the GBOV LAI reference (Fig. 14). MQA was used to measure the quality of LAI retrievals. The effect of introducing quality into the algorithm [Fig. 14(a)] was significantly better than that of not considering quality information [Fig. 14(b)]. Assigning different weights according to the MQA can alleviate the uncertainty caused by low-quality retrievals. In other words, it is necessary to consider the quality of the retrievals when using these products. Moreover, using a single feature [Fig. 14(b-1)], Fig. 14(b-2) is not ideal compared with multiple information compositing [Fig. 14(b-3)]. Using single spatial information performed worst, indicating that spatial correlation cannot be applied alone to spatial improvements on large scales [79]. However, considering both spatial and temporal information [Fig. 14(b-3)] can break through the limitation of a single feature. Several studies support the idea that integrating multiple information has advantages over using a single feature [49], [50], [52]. Furthermore, it is important to note that the use of spatial and temporal information in the algorithm is completely independent. This means that the values derived from employing spatial information do not impact the results of the temporal correlation. When using both types of information sequentially, the uncertainty of the initial calculation will directly impact subsequent results, regardless of which type of information is used first. However, we mitigate this uncertainty by independently utilizing spatial and temporal correlation and integrating multiple sources of information with respective weights, which can effectively alleviate this uncertainty. Notably, STICA handles outliers [red circles in Fig. 14(b-3)] better than the simple average. The proposed STICA has three distinct improvements over the simple average. First, a new pixel quality classification, MQA, is obtained by accessing multiple aspects of pixel uncertainties; different weights are assigned to the pixels according to the MQA. Second, the spatiotemporal information of LAI, the raw MODIS LAI information, and MQA information are used simultaneously in our approach. Third, multiple information is integrated based on the TSS to assign weights.

There are some uncertainties in the classification of the auxiliary MODIS land cover data [77] that we used in the algorithm, which could impact the accuracy of our algorithm. For remote sensing products, an uncertainty analysis must cover typical land surfaces and involve long time series to accurately reflect the accuracy and spatiotemporal stability [80]. From the perspective of minimizing noisy fluctuations and improving time-series smoothness, the STICA performs better than the raw MODIS LAI over all eight biome types. However, STICA's performance on long time series was not analyzed. We expect to expand the MODIS LAI reanalyzed product over a larger area or even globally using this algorithm

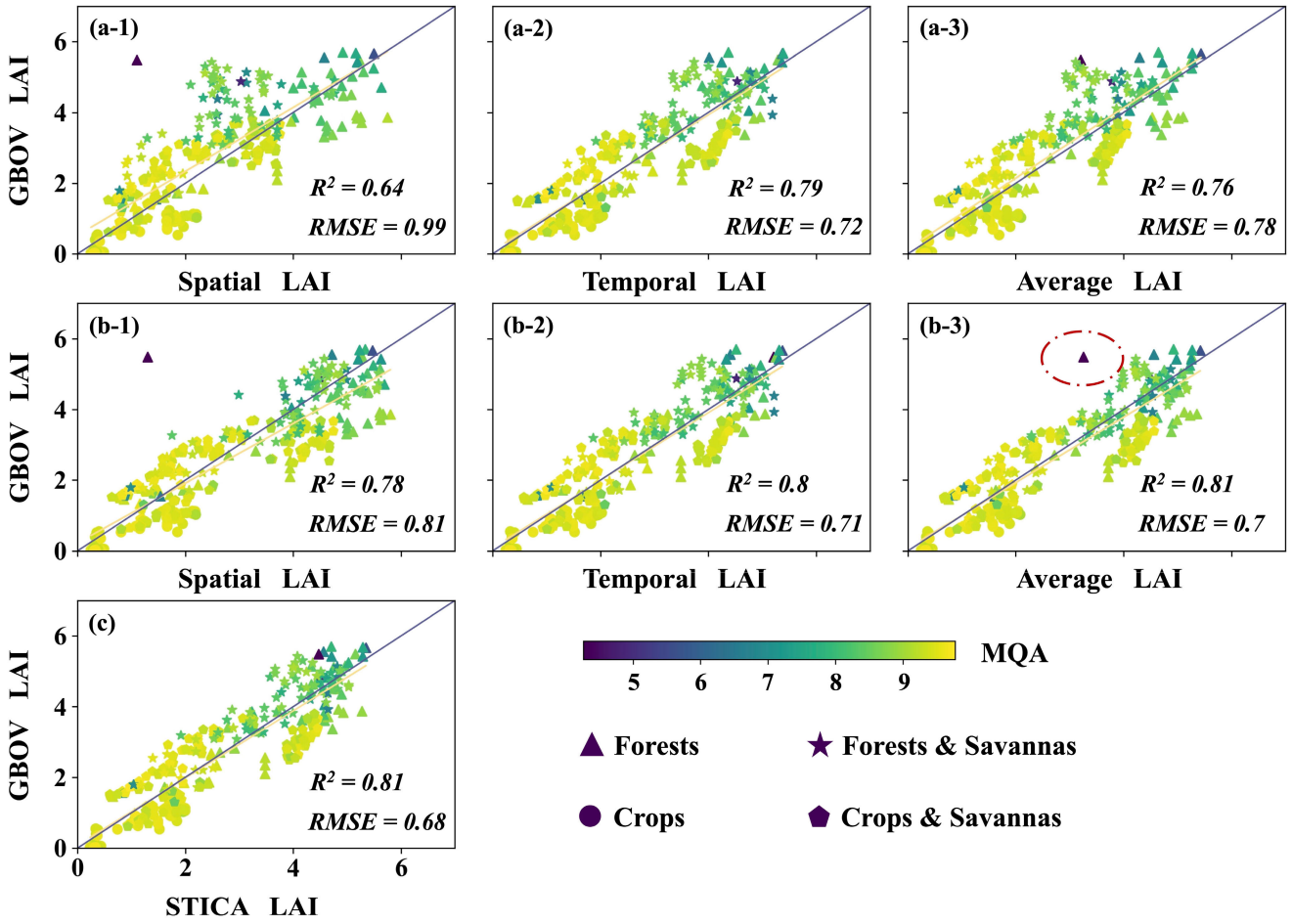

Fig. 14. Scatterplots of GBOV site validation under different information combinations: (a) MQA of each pixel was not considered in the calculation; (a-1) and (b-1) employed only spatial information; (a-2) and (b-2) employed only temporal information; (a-3) and (b-3) represent the simple average of temporal and spatial information; and (c) weighted average of multiple information. The color of symbols corresponds to MQA ranging from 4 (poor) to 10 (good), and the shape of the symbols represents different biome types.

due to the operational potential. A more comprehensive evaluation and validation analysis of STICA will be planned as a next step, including the global scale intercomparison with other LAI products, direct validation with globally covered site measurements, and indirect verification with temperature, precipitation, and extreme events.

V. Conclusion

MODIS LAI is calculated independently on a pixel and daily basis without using any spatiotemporal correlation information, which causes an increased noise level in this product. Hence, in some cases, this product does not meet the uncertainty requirements presented by GCOS, limiting its applications. Here, we proposed STICA that directly introduces prior spatiotemporal correlation and MQA information into the existing MODIS LAI product, thus maintaining it consistent with the original physically based MODIS LAI production. The algorithm was evaluated and validated with simulated dataset and ground-based LAI reference. The performance of our algorithm was tested in different biome types, particularly in the Amazon forest region, where atmospheric conditions often introduce artifacts to current LAI products. The results denote that STICA LAI performs better than the raw MODIS LAI. The simulated LAI shows that the RMSE of STICA was in general small, and the mean RMSE of SUA and STICA were 0.44 and 0.23, respectively. Based on the GBOV ground-based LAI reference, the R^2 increases from 0.79 to 0.81 and the RMSE decreased from 0.81 to 0.68. STICA performed better in sites with pure vegetation type than hybrid type. The improvements in LAI retrievals were more evident as the classification quality degraded. In addition, this article employed TSS and TSA to quantify the fluctuation and anomaly of time series, respectively. The STICA method effectively reduced noisy fluctuations and exhibited smoother time series among eight biome types, with a reduction of more than 50% in the average of TSS from raw to STICA. In the Amazon forest region, the STICA significantly improved the consistency of LAI time-series data, as evidenced by a drastic increase in the proportion of pixels with TSS less than 10, from 5.79% to 99.31%, and a notable improvement in the ratio of pixels with TSA less than 10, from 6.34% to 97.57%. STICA also successfully eliminates abnormal LAI declines and correcting extreme LAI outliers. By incorporating spatiotemporal correlation information and MQA information, STICA surpasses the limitations of relying on a single feature, resulting in less anomalous LAI and high-quality retrievals.

Due to the operational potential of this algorithm, a reanalyzed MODIS LAI product with global coverage generated by our method can likely provide substantial benefits to applications that rely on high-quality and stable LAI retrievals.

APPENDIX

A. Site Information for GBOV

See Table I.

B. Definition of TSS

$$\text{Absolute TSS}(t) = \frac{\left| \begin{array}{c} (X(t_{n+1}) - X(t_{n-1})) \times t_n - X(t_n) \times (t_{n+1} - t_{n-1}) \\ -(X(t_{n+1}) - X(t_{n-1})) \times t_{n-1} + X(t_{n-1}) \times (t_{n+1} - t_{n-1}) \end{array} \right|}{\sqrt{(X(t_{n+1}) - X(t_{n-1}))^2 + (t_{n+1} - t_{n-1})^2}} \tag{13}$$

$$\text{Relative TSS}(t) = \frac{\text{absolute TSS}(t)}{\text{LAI}(t)} \tag{14}$$

where $X(t_n)$ is the LAI value at target moment t. $X(t_{n+1})$ and $X(t_{n-1})$ are the adjacent time-series data obtained at the previous moment and the next moment, respectively.

C. Calibration of the Proportions of Main and Backup Algorithm

See Table IV.

D. Parameters Configuration When Employing Spatial Information

See Fig. 12.

E. Parameters Configuration When Employing Temporal Information

See Fig. 13.

REFERENCES

[1] J. M. Chen and T. A. Black, "Defining leaf area index for non-flat leaves," *Plant, Cell Environ.*, vol. 15, no. 4, pp. 421–429, May 1992, doi: 10.1111/j.1365-3040.1992.tb00992.x.

[2] Y. Knyazikhin, J. V. Martonchik, R. B. Myneni, D. J. Diner, and S. W. Running, "Synergistic algorithm for estimating vegetation canopy leaf area index and fraction of absorbed photosynthetically active radiation from MODIS and MISR data," *J. Geophys. Res., Atmos.*, vol. 103, no. D24, pp. 32257–32275, 1998, doi: 10.1029/98JD02462.

[3] Y. Knyazikhin, "MODIS leaf area index (LAI) and fraction of photo synthetically active radiation absorbed by vegetation (FPAR) product (MOD 15) algorithm theoretical basis document," 1999. [Online]. Available: https://modis.gsfc.nasa.gov/data/atbd/atbd_mod15.pdf

[4] S. Boussetta, G. Balsamo, A. Beljaars, T. Kral, and L. Jarlan, "Impact of a satellite-derived leaf area index monthly climatology in a global numerical weather prediction model," *Int. J. Remote Sens.*, vol. 34, nos. 9–10, pp. 3520–3542, May 2013, doi: 10.1080/01431161.2012.716543.

[5] A. D. Richardson, T. F. Keenan, M. Migliavacca, Y. Ryu, O. Sonnentag, and M. Toomey, "Climate change, phenology, and phenological control of vegetation feedbacks to the climate system," *Agricult. Forest Meteorol.*, vol. 169, pp. 156–173, Feb. 2013, doi: 10.1016/j.agrformet.2012.09.012.

[6] A. Tillack, A. Clasen, B. Kleinschmit, and M. Förster, "Estimation of the seasonal leaf area index in an alluvial forest using high-resolution satellite-based vegetation indices," *Remote Sens. Environ.*, vol. 141, pp. 52–63, Feb. 2014, doi: 10.1016/j.rse.2013.10.018.

[7] P. J. Sellers et al., "Modeling the exchanges of energy, water, and carbon between continents and the atmosphere," *Science*, vol. 275, no. 5299, pp. 502–509, 1997, doi: 10.1126/science.275.5299.502.

[8] C. Chen et al., "Biophysical impacts of Earth greening largely controlled by aerodynamic resistance," *Sci. Adv.*, vol. 6, no. 47, pp. 1–10, Nov. 2020, doi: 10.1126/sciadv.abb1981.

[9] K. Yan et al., "A bibliometric visualization review of the MODIS LAI/FPAR products from 1995 to 2020," *J. Remote Sens.*, vol. 2021, pp. 1–20, Jan. 2021, doi: 10.34133/2021/7410921.

[10] R. B. Myneni et al., "Global products of vegetation leaf area and fraction absorbed PAR from year one of MODIS data," *Remote Sens. Environ.*, vol. 83, nos. 1–2, pp. 214–231, Nov. 2002, doi: 10.1016/S0034-4257(02)00074-3.

[11] F. Baret et al., "GEOV1: LAI and FAPAR essential climate variables and FCOVER global time series capitalizing over existing products. Part 1: Principles of development and production," *Remote Sens. Environ.*, vol. 137, pp. 299–309, Oct. 2013, doi: 10.1016/j.rse.2012.12.027.

[12] H. Ma and S. Liang, "Development of the GLASS 250-m leaf area index product (version 6) from MODIS data using the bidirectional LSTM deep learning model," *Remote Sens. Environ.*, vol. 273, May 2022, Art. no. 112985, doi: 10.1016/j.rse.2022.112985.

[13] J. Pisek and J. M. Chen, "Comparison and validation of MODIS and VEGETATION global LAI products over four BigFoot sites in North America," *Remote Sens. Environ.*, vol. 109, no. 1, pp. 81–94, Jul. 2007, doi: 10.1016/j.rse.2006.12.004.

[14] K. Yan et al., "Evaluation of MODIS LAI/FPAR product collection 6. Part 2: Validation and intercomparison," *Remote Sens.*, vol. 8, no. 6, p. 460, May 2016, doi: 10.3390/rs8060460.

[15] J. Mao, X. Shi, P. Thornton, F. Hoffman, Z. Zhu, and R. Myneni, "Global latitudinal-asymmetric vegetation growth trends and their driving mechanisms: 1982–2009," *Remote Sens.*, vol. 5, no. 3, pp. 1484–1497, Mar. 2013, doi: 10.3390/rs5031484.

[16] C. Chen et al., "China and India lead in greening of the world through land-use management," *Nature Sustainability*, vol. 2, no. 2, pp. 122–129, Feb. 2019, doi: 10.1038/s41893-019-0220-7.

[17] L. Chen and P. A. Dirmeyer, "Adapting observationally based metrics of biogeophysical feedbacks from land cover/land use change to climate modeling," *Environ. Res. Lett.*, vol. 11, no. 3, Mar. 2016, Art. no. 034002, doi: 10.1088/1748-9326/11/3/034002.

[18] Z. Zhu et al., "Greening of the Earth and its drivers," *Nature Climate Change*, vol. 6, no. 8, pp. 791–795, 2016, doi: 10.1038/nclimate3004.

[19] K. Yan et al., "Evaluation of MODIS LAI/FPAR product collection 6. Part 1: Consistency and improvements," *Remote Sens.*, vol. 8, no. 5, pp. 1–16, 2016, doi: 10.3390/rs8050359.

[20] W. Yang et al., "Analysis of leaf area index products from combination of MODIS Terra and Aqua data," *Remote Sens. Environ.*, vol. 104, no. 3, pp. 297–312, 2006, doi: 10.1016/j.rse.2006.04.016.

[21] X. Li et al., "Assimilating leaf area index of three typical types of subtropical forest in China from MODIS time series data based on the integrated ensemble Kalman filter and PROSAIL model," *ISPRS J. Photogramm. Remote Sens.*, vol. 126, pp. 68–78, Apr. 2017, doi: 10.1016/j.isprsjprs.2017.02.002.

[22] Z. Xiao, S. Liang, J. Wang, J. Song, and X. Wu, "A temporally integrated inversion method for estimating leaf area index from MODIS data," *IEEE Trans. Geosci. Remote Sens.*, vol. 47, no. 8, pp. 2536–2545, Aug. 2009, doi: 10.1109/TGRS.2009.2015656.

[23] X. Li et al., "Assimilating spatiotemporal MODIS LAI data with a particle filter algorithm for improving carbon cycle simulations for bamboo forest ecosystems," *Sci. Total Environ.*, vol. 694, Dec. 2019, Art. no. 133803, doi: 10.1016/j.scitotenv.2019.133803.

[24] C. Guillemot and O. Le Meur, "Image inpainting: Overview and recent advances," *IEEE Signal Process. Mag.*, vol. 31, no. 1, pp. 127–144, Jan. 2014, doi: 10.1109/MSP.2013.2273004.

[25] H. Mitášová and J. Hofierka, "Interpolation by regularized spline with tension: II. Application to terrain modeling and surface geometry analysis," *Math. Geol.*, vol. 25, no. 6, pp. 657–669, 1993, doi: 10.1007/BF00893172.

[26] P. R. Smith, "Bilinear interpolation of digital images," *Ultramicroscopy*, vol. 6, no. 2, pp. 201–204, 1981.

[27] G. Y. Lu and D. W. Wong, "An adaptive inverse-distance weighting spatial interpolation technique," *Comput. Geosci.*, vol. 34, no. 9, pp. 1044–1055, 2008, doi: 10.1016/j.cageo.2007.07.010.

[28] M. L. Stein, *Interpolation of Spatial Data: Some Theory for Kriging*. New York, NY, USA: Springer, 2012.

[29] M. Bertalmio, G. Sapiro, V. Caselles, and C. Ballester, "Image inpainting," in *Proc. 27th Annu. Conf. Comput. Graph. Interact. Techn.*, 2000, pp. 417–424, doi: 10.1145/344779.344972.

[30] A. Criminisi, P. Pérez, and K. Toyama, "Region filling and object removal by exemplar-based image inpainting," *IEEE Trans. Image Process.*, vol. 13, no. 9, pp. 1200–1212, Sep. 2004, doi: 10.1109/TIP.2004.833105.

[31] Q. Cheng, H. Shen, L. Zhang, and P. Li, "Inpainting for remotely sensed images with a multichannel nonlocal total variation model," *IEEE Trans. Geosci. Remote Sens.*, vol. 52, no. 1, pp. 175–187, Jan. 2014, doi: 10.1109/TGRS.2012.2237521.

[32] F. Gao et al., "An algorithm to produce temporally and spatially continuous MODIS-LAI time series," *IEEE Geosci. Remote Sens. Lett.*, vol. 5, no. 1, pp. 60–64, Jan. 2008, doi: 10.1109/LGRS.2007.907971.

[33] H. Fang, S. Liang, J. R. Townshend, and R. E. Dickinson, "Spatially and temporally continuous LAI data sets based on an integrated filtering method: Examples from North America," *Remote Sens. Environ.*, vol. 112, no. 1, pp. 75–93, Jan. 2008, doi: 10.1016/j.rse.2006.07.026.

[34] X. Zhang, "Reconstruction of a complete global time series of daily vegetation index trajectory from long-term AVHRR data," *Remote Sens. Environ.*, vol. 156, pp. 457–472, Nov. 2015, doi: 10.1016/j.rse.2014.10.012.

[35] B. N. Holben, "Characteristics of maximum-value composite images from temporal AVHRR data," *Int. J. Remote Sens.*, vol. 7, no. 11, pp. 1417–1434, 1986, doi: 10.1080/01431168608948945.

[36] N. Viovy, O. Arino, and A. Belward, "The best index slope extraction (BISE): A method for reducing noise in NDVI time-series," *Int. J. Remote Sens.*, vol. 13, no. 8, pp. 1585–1590, 1992, doi: 10.1080/01431169208904212.

[37] G. Deslauriers and S. Dubuc, "Symmetric iterative interpolation processes," *Constructive Approximation*, vol. 5, no. 1, pp. 49–68, Dec. 1989, doi: 10.1007/BF01889598.

[38] J. Chen et al., "A simple method for reconstructing a high-quality NDVI time-series data set based on the Savitzky–Golay filter," *Remote Sens. Environ.*, vol. 91, nos. 3–4, pp. 332–344, Jun. 2004, doi: 10.1016/j.rse.2004.03.014.

[39] P. Jönsson and L. Eklundh, "TIMESAT—A program for analyzing time-series of satellite sensor data," *Comput. Geosci.*, vol. 30, no. 8, pp. 833–845, Oct. 2004, doi: 10.1016/j.cageo.2004.05.006.

[40] P. Jonsson and L. Eklundh, "Seasonality extraction by function fitting to time-series of satellite sensor data," *IEEE Trans. Geosci. Remote Sens.*, vol. 40, no. 8, pp. 1824–1832, Aug. 2002, doi: 10.1109/TGRS.2002.802519.

[41] P. S. A. Beck, C. Atzberger, K. A. Høgda, B. Johansen, and A. K. Skidmore, "Improved monitoring of vegetation dynamics at very high latitudes: A new method using MODIS NDVI," *Remote Sens. Environ.*, vol. 100, no. 3, pp. 321–334, 2006, doi: 10.1016/j.rse.2005.10.021.

[42] J. Zhou, L. Jia, and M. Menenti, "Reconstruction of global MODIS NDVI time series: Performance of harmonic analysis of time series (HANTS)," *Remote Sens. Environ.*, vol. 163, pp. 217–228, Jun. 2015.

[43] Y. Yang, J. Luo, Q. Huang, W. Wu, and Y. Sun, "Weighted double-logistic function fitting method for reconstructing the high-quality Sentinel-2 NDVI time series data set," *Remote Sens.*, vol. 11, no. 20, pp. 1–18, 2019, doi: 10.3390/rs11202342.

[44] Z. Ao, Y. Sun, and Q. Xin, "Constructing 10-m NDVI time series from Landsat 8 and sentinel 2 images using convolutional neural networks," *IEEE Geosci. Remote Sens. Lett.*, vol. 18, no. 8, pp. 1461–1465, Aug. 2021, doi: 10.1109/LGRS.2020.3003322.

[45] M. Das and S. K. Ghosh, "A deep-learning-based forecasting ensemble to predict missing data for remote sensing analysis," *IEEE J. Sel. Topics Appl. Earth Observ. Remote Sens.*, vol. 10, no. 12, pp. 5228–5236, Dec. 2017, doi: 10.1109/JSTARS.2017.2760202.

[46] A. Htitiou, A. Boudhar, and T. Benabdelouahab, "Deep learning-based spatiotemporal fusion approach for producing high-resolution NDVI time-series datasets," *Can. J. Remote Sens.*, vol. 47, no. 2, pp. 182–197, Mar. 2021, doi: 10.1080/07038992.2020.1865141.

[47] Q. Wang, L. Wang, X. Zhu, Y. Ge, X. Tong, and P. M. Atkinson, "Remote sensing image gap filling based on spatial–spectral random forests," *Sci. Remote Sens.*, vol. 5, Jun. 2022, Art. no. 100048, doi: 10.1016/j.srs.2022.100048.

[48] H. Shen et al., "Missing information reconstruction of remote sensing data: A technical review," *IEEE Geosci. Remote Sens. Mag.*, vol. 3, no. 3, pp. 61–85, Sep. 2015, doi: 10.1109/MGRS.2015.2441912.

[49] H. Fang et al., "Developing a spatially continuous 1 km surface albedo data set over North America from Terra MODIS products," *J. Geophys. Res.*, vol. 112, no. D20, 2007, Art. no. D20206, doi: 10.1029/2006JD008377.

[50] R. Cao et al., "A simple method to improve the quality of NDVI time-series data by integrating spatiotemporal information with the Savitzky–Golay filter," *Remote Sens. Environ.*, vol. 217, pp. 244–257, Nov. 2018, doi: 10.1016/j.rse.2018.08.022.

[51] S. K. Padhee and S. Dutta, "Spatio-temporal reconstruction of MODIS NDVI by regional land surface phenology and harmonic analysis of time-series," *GISci. Remote Sens.*, vol. 56, no. 8, pp. 1261–1288, Nov. 2019, doi: 10.1080/15481603.2019.1646977.

[52] D. Chu et al., "Long time-series NDVI reconstruction in cloud-prone regions via spatio-temporal tensor completion," *Remote Sens. Environ.*, vol. 264, Oct. 2021, Art. no. 112632, doi: 10.1016/j.rse.2021.112632.

[53] J. Borak and M. Jasinski, "Effective interpolation of incomplete satellite-derived leaf-area index time series for the continental United States," *Agricult. Forest Meteorol.*, vol. 149, no. 2, pp. 320–332, Feb. 2009, doi: 10.1016/j.agrformet.2008.08.017.

[54] T. Pede and G. Mountrakis, "An empirical comparison of interpolation methods for MODIS 8-day land surface temperature composites across the conterminous Unites States," *ISPRS J. Photogramm. Remote Sens.*, vol. 142, pp. 137–150, Aug. 2018, doi: 10.1016/j.isprsjprs.2018.06.003.

[55] S. Ganguly, M. A. Friedl, B. Tan, X. Zhang, and M. Verma, "Land surface phenology from MODIS: Characterization of the collection 5 global land cover dynamics product," *Remote Sens. Environ.*, vol. 114, no. 8, pp. 1805–1816, Aug. 2010, doi: 10.1016/j.rse.2010.04.005.

[56] D. Sulla-Menashe and M. A. Friedl, "User guide to collection 6 MODIS land cover (MCD12Q1 and MCD12C1) product," USGS, Reston, VA, USA, 2018, p. 18. [Online]. Available: http://girps.net/wp-content/uploads/2019/03/MCD12_User_Guide_V6.pdf

[57] J. Pu et al., "Evaluation of the MODIS LAI/FPAR algorithm based on 3D-RTM simulations: A case study of grassland," *Remote Sens.*, vol. 12, no. 20, pp. 1–17, 2020, doi: 10.3390/rs12203391.

[58] K. Yan et al., "Generating global products of LAI and FPAR from SNPP-VIIRS data: Theoretical background and implementation," *IEEE Trans. Geosci. Remote Sens.*, vol. 56, no. 4, pp. 2119–2137, Apr. 2018, doi: 10.1109/TGRS.2017.2775247.

[59] R. Myneni, Y. Knyazikhin, and T. Park, "MOD15A2H MODIS/Terra leaf area index/FPAR 8-day L4 global 500 m SIN grid V006," NASA EOSDIS Land Processes DAAC, 2015.

[60] R. Myneni, "MODIS collection 6(C6) LAI/FPAR product user's guide," Tech. Rep., 2020, vol. 6. [Online]. Available: https://lpdaac.usgs.gov/documents/90/MOD15_ATBD.pdf

[61] G. Bai et al., "GBOV (ground-based observation for validation): A Copernicus service for validation of vegetation land products," in *Proc. IEEE Int. Geosci. Remote Sens. Symp.*, Jul. 2019, pp. 4592–4594, doi: 10.1109/IGARSS.2019.8898634.

[62] L. A. Brown et al., "Evaluation of global leaf area index and fraction of absorbed photosynthetically active radiation products over North America using Copernicus ground based observations for validation data," *Remote Sens. Environ.*, vol. 247, Sep. 2020, Art. no. 111935, doi: 10.1016/j.rse.2020.111935.

[63] Y. Wenze et al., "MODIS leaf area index products: From validation to algorithm improvement," *IEEE Trans. Geosci. Remote Sens.*, vol. 44, no. 7, pp. 1885–1896, Jul. 2006, doi: 10.1109/TGRS.2006.871215.

[64] D. Zou et al., "Revisit the performance of MODIS and VIIRS leaf area index products from the perspective of time-series stability," *IEEE J. Sel. Topics Appl. Earth Observ. Remote Sens.*, vol. 15, pp. 8958–8973, 2022, doi: 10.1109/JSTARS.2022.3214224.

[65] D. C. Montgomery, L. A. Johnson, and J. S. Gardiner, *Forecasting and Time Series Analysis*. New York, NY, USA: McGraw-Hill, 1990.

[66] E. Ostertagová and O. Ostertag, "Forecasting using simple exponential smoothing method," *Acta Electrotechnica et Inf.*, vol. 12, no. 3, pp. 62–66, Jan. 2012, doi: 10.2478/v10198-012-0034-2.

[67] E. S. Gardner, "Exponential smoothing: The state of the art—Part II," *Int. J. Forecasting*, vol. 22, no. 4, pp. 637–666, Oct. 2006, doi: 10.1016/j.ijforecast.2006.03.005.

[68] X. Yi, Z. Yu, Z. Junbo, and T. Li, "ST-MVL: Filling missing values in geo-sensory time series data," *Proc. Int. Joint Conf. Artif. Intell. (IJCAI)*, Jan. 2016, pp. 2704–2710.

[69] E. L. Bullock, C. E. Woodcock, C. Souza, and P. Olofsson, "Satellite-based estimates reveal widespread forest degradation in the Amazon," *Global Change Biol.*, vol. 26, no. 5, pp. 2956–2969, May 2020, doi: 10.1111/gcb.15029.

[70] D. I. Rappaport, D. C. Morton, M. Longo, M. Keller, R. Dubayah, and M. N. Dos-Santos, "Quantifying long-term changes in carbon stocks and forest structure from Amazon forest degradation," *Environ. Res. Lett.*, vol. 13, no. 6, Jun. 2018, Art. no. 065013, doi: 10.1088/1748-9326/aac331.

[71] T. Hilker et al., "On the measurability of change in Amazon vegetation from MODIS," *Remote Sens. Environ.*, vol. 166, pp. 233–242, Sep. 2015, doi: 10.1016/j.rse.2015.05.020.

[72] H. Hashimoto et al., "New generation geostationary satellite observations support seasonality in greenness of the Amazon evergreen forests," *Nature Commun.*, vol. 12, no. 1, p. 684, Jan. 2021, doi: 10.1038/s41467-021-20994-y.

[73] S. Garrigues et al., "Validation and intercomparison of global leaf area index products derived from remote sensing data," *J. Geophys. Res., Biogeosci.*, vol. 113, no. G2, Jun. 2008, Art. no. G02028, doi: 10.1029/2007JG000635.

[74] X. Xie et al., "Revisiting dry season vegetation dynamics in the Amazon rainforest using different satellite vegetation datasets," *Agricult. Forest Meteorol.*, vol. 312, Jan. 2022, Art. no. 108704, doi: 10.1016/j.agrformet.2021.108704.

[75] J. Heiskanen et al., "Seasonal variation in MODIS LAI for a boreal forest area in Finland," *Remote Sens. Environ.*, vol. 126, pp. 104–115, Nov. 2012, doi: 10.1016/j.rse.2012.08.001.

[76] Y. Qu, A. Shaker, C. Silva, C. Klauberg, and E. Pinagé, "Remote sensing of leaf area index from LiDAR height percentile metrics and comparison with MODIS product in a selectively logged tropical forest area in eastern Amazonia," *Remote Sens.*, vol. 10, no. 6, p. 970, Jun. 2018, doi: 10.3390/rs10060970.

[77] H. L. Fang, W. J. Li, and R. B. Myneni, "The impact of potential land cover misclassification on MODIS leaf area index (LAI) estimation: A statistical perspective," *Remote Sens.*, vol. 5, no. 2, pp. 830–844, Feb. 2013, doi: 10.3390/rs5020830.

[78] M. N. Smith et al., "Seasonal and drought-related changes in leaf area profiles depend on height and light environment in an Amazon forest," *New Phytol.*, vol. 222, no. 3, pp. 1284–1297, May 2019, doi: 10.1111/nph.15726.

[79] S. Li, L. Xu, Y. Jing, H. Yin, X. Li, and X. Guan, "High-quality vegetation index product generation: A review of NDVI time series reconstruction techniques," *Int. J. Appl. Earth Observ. Geoinf.*, vol. 105, Dec. 2021, Art. no. 102640, doi: 10.1016/j.jag.2021.102640.

[80] W. Buermann, "Analysis of a multiyear global vegetation leaf area index data set," *J. Geophys. Res.*, vol. 107, no. D22, pp. 14-1–14-16, 2002, doi: 10.1029/2001JD000975.

Jingrui Wang was born in Sichuan, China. She is currently pursuing the M.E. degree in remote sensing with the China University of Geosciences, Beijing, China, under the direction of Dr. Kai Yan.

Her research interests include vegetation remote sensing, particularly in the retrieval of vegetation parameter and leaf area index (LAI) product processing.

Kai Yan received the B.S. degree in mapping and surveying from the Beijing University of Civil Engineering and Architecture, Beijing, China, in 2011, and the Ph.D. degree in geographic information system (GIS)/remote sensing (RS) from Beijing Normal University, Beijing, in 2018.

He was a Visiting Scholar with the Department of Earth and Environment, Boston University, Boston, MA, USA, from 2014 to 2016, and an Assistant Professor with the School of Land Science and Techniques, China University of Geosciences, Beijing. He is currently an Assistant Professor with the Faculty of Geographical Science, Beijing Normal University. He has been involved in the generation and assessment of official MODIS/VIIRS global leaf area index (LAI) and the fraction of photosynthetically active radiation absorbed by vegetation (FPAR) products. His current research interests include the bidirectional reflectance distribution function (BRDF) modeling, and LAI and FPAR mapping.

Si Gao was born in Henan, China. She is currently pursuing the M.E. degree in remote sensing with the China University of Geosciences, Beijing, China, under the direction of Dr. Kai Yan.

Her research interests include vegetation remote sensing, particularly in the retrieval of vegetation parameter.

Jiabin Pu was born in Zhejiang, China. He received the M.E. degree from the China University of Geosciences, Beijing, China, in 2022. He is currently pursuing the Ph.D. degree in geography with the Department of Earth and Environment, Boston University, Boston, MA, USA.

His research interests include remote sensing of vegetation.

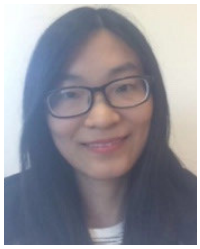

Jinxiu Liu received the M.Sc. degree in geographic information system (GIS) from Beijing Normal University, Beijing, China, in 2013, and the Ph.D. degree in geography from the University of Helsinki, Helsinki, Finland, in 2017.

She is currently a Lecturer with the School of Information Engineering, China University of Geosciences, Beijing. Her research interests include time-series analysis with dense satellite data and vegetation remote sensing.

Taejin Park received the Ph.D. degree in geography from the Department of Earth and Environment, Boston University, Boston, MA, USA, in 2019.

He is currently a Research Scientist at Bay Area Environmental Research Institute and NASA Ames Research Center, Moffett Field, CA, USA. His research interests include the remote sensing of vegetation and climate vegetation interactions.

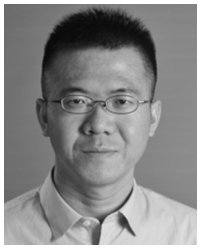

Jian Bi received the M.Sc. degree in geographic information system (GIS) from Beijing Normal University, Beijing, China, in 2011, and the Ph.D. degree in geography from Boston University, Boston, MA, USA, in 2015.

He is currently an Associate Professor with Lanzhou University, Lanzhou, China. His research interests include remote sensing of vegetation dynamics, time-series analysis in remote sensing, and climate change.

Eduardo Eiji Maeda received the M.Sc. degree in remote sensing from the National Institute for Space Research (INPE), São José dos Campos, Brazil, in 2008, and the Ph.D. degree in geography from the University of Helsinki, Helsinki, Finland, in 2011.

He is currently an Associate Professor with the University of Helsinki and also with the Finnish Meteorological Institute, Helsinki. He currently leads the Terrestrial Ecosystem Dynamics Laboratory (TreeD lab), Department of Geosciences and Geography, University of Helsinki.

Janne Heiskanen received the M.Sc. degree in geography from the University of Turku, Turku, Finland, in 2003, and the Ph.D. degree in geography from the University of Helsinki, Helsinki, Finland, in 2008.

He is currently a University Researcher with the Department of Geosciences and Geography, University of Helsinki. His research interests include remote sensing of vegetation parameters, land cover change, and water and carbon cycles.

Yuri Knyazikhin received the M.S. degree in applied mathematics from Tartu University, Tartu, Estonia, in 1978, and the Ph.D. degree in numerical analysis from the N. I. Muskhelishvilli Institute of Computing Mathematics, Georgian Academy of Sciences, Tbilisi, Georgia, in 1985.

He was a Research Scientist with the Institute of Astrophysics and Atmospheric Physics, Tartu University, and also with the Computer Center of the Siberian Branch, Russian Academy of Sciences, Moscow, Russia, from 1978 to 1990. He worked with the University of Göttingen, Göttingen, Germany, from 1990 to 1996. He was an Alexander von Humboldt Fellow from 1992 to 1993. He is currently a Research Professor with the Department of Geography, Boston University, Boston, MA, USA. His work was published in the areas of numerical integral and differential equations, theory of radiative transfer in atmospheres and plant canopies, remote sensing of the atmosphere and plant canopies, ground-based radiation measurements, forest ecosystem dynamics, and modeling multifunctional forest management.

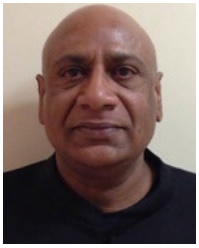

Ranga B. Myneni received the Ph.D. degree in biology from the University of Antwerp, Antwerp, Belgium, in 1985.

He is currently a Professor with Boston University, Boston, MA, USA. He is a Science Team Member of NASA Moderate Resolution Imaging Spectroradiometer (MODIS) and VIIRS projects. He has authored over 330 scientific articles in peer-refereed journals and authored or coauthored over 250 scientific articles in peer-refereed journals. He is a Highly Cited Researcher in geosciences and in environment and ecology for four years running since 2019. His research interests include remote sensing of vegetation and climate–vegetation interactions.